Check for updates

Accepted Article

A Global High-resolution Mesoscale Convective System Database using Satellite-derived Cloud Tops, Surface Precipitation, and Tracking

Zhe Feng[1], L. Ruby Leung[1], Nana Liu[1], Jingyu Wang[1], Robert A. Houze Jr.[2], Jianfeng Li[1], Joseph C. Hardin[1], Dandan Chen[3], Jianping Guo[3]

[1] Atmospheric Sciences and Global Change Division, Pacific Northwest National Laboratory, Richland, WA, USA.

[2] Department of Atmospheric Sciences, University of Washington, Seattle, WA, USA

[3] State Key Laboratory of Severe Weather, Chinese Academy of Meteorological Sciences, Beijing 100081, China.

Corresponding author: Zhe Feng (zhe.feng@pnnl.gov)

Key Points:

- Develop an algorithm to track mesoscale convective systems globally using satellite infrared brightness temperature and precipitation data
- Satellite-based tracking reproduces mesoscale convective system statistics derived from tracking using ground-based radar network data
- Global mesoscale convective system characteristics and their regional and seasonal variabilities are presented

This article has been accepted for publication and undergone full peer review but has not been through the copyediting, typesetting, pagination and proofreading process, which may lead to differences between this version and the Version of Record. Please cite this article as doi: 10.1029/2020JD034202.

This article is protected by copyright. All rights reserved.

Accepted Article

Abstract

A new methodology is developed to construct a global (60°S–60°N) long-term (2000-2019) high-resolution (~10-km, hourly) mesoscale convective system (MCS) database by tracking MCS jointly using geostationary satellite infrared brightness temperature (T_b) and precipitation feature (PF) characteristics from the Integrated Multi-satellitE Retrievals for GPM (IMERG) precipitation datasets. Independent validation shows that the satellite-based MCS dataset is able to reproduce important MCS statistics derived from ground-based radar network observations in the U.S. and China. We show that by carefully considering key PF characteristics in addition to T_b signatures, the new method significantly improves upon previous T_b-only methods in detecting MCSs in the midlatitudes for all seasons. Results show that MCSs account for over 50% of annual total rainfall across most of the tropical belt and in select regions of the midlatitudes, with a strong seasonality over many regions of the globe. The tracking database allows Lagrangian aspects such as MCS lifetime and translational speed and direction to be analyzed. The longest-lived MCSs preferentially occur over the subtropical oceans. The land MCSs have higher cloud-tops associated with more intense convection, and oceanic MCSs have much higher rainfall production. While MCSs are observed in many regions of the globe, there are fundamental differences in their dynamic and thermodynamic structures that warrant better understanding of processes that control their evolution. This global database provides significant opportunities for observational and modeling studies of MCSs, their characteristics and roles in regional and global water and energy cycles, as well as their hydrologic and other impacts.

Plain Language Summary

Convective storms of mesoscale dimension are a key component in the Earth's energy and hydrological cycle. Mesoscale storms grow to hundreds of kilometers in size and can last for more than a day, and produce a majority of the annual rainfall in many regions of the world. Past studies of mesoscale storms have been limited to the tropics and used methodologies not appropriate in the midlatitudes. Here, we develop a new methodology to track mesoscale storms globally using high-resolution satellite observations of both cloud and precipitation. The satellite-based storm tracking reproduces important storm statistics derived from ground-based radar observations. Our new method significantly improves the detection of mesoscale storms in the midlatitudes. This new storm tracking database is the first to cover both the tropics and midlatitudes for all seasons. Results show that mesoscale convective storms account for over 50% annual rainfall across the tropics and many regions of the subtropics and midlatitudes. Storms over land have more intense convection, while those over ocean produce heavier rainfall and last longer. This global mesoscale storms tracking database supports a broad range of applications such as their role in global extreme rainfall and the evaluation of global weather and climate model simulations.

This article is protected by copyright. All rights reserved.

1 Introduction

Deep convection, especially when it takes on mesoscale dimensions, plays an important role in the global energy and hydrological cycle. Mesoscale convective system (MCS) is the largest form taken by individual convective cloud systems. It consists of an ensemble of cumulonimbus towers that produce a contiguous precipitation area of 100 km or larger (Houze, 2004; 2014 Chapter 9; Houze, 2018). MCSs are ubiquitous in the tropics, particularly over the west Pacific warm pool, the intertropical convergence zone (ITCZ), tropical Africa, and the Amazon (Laing & Fritsch, 1997; Yuan & Houze, 2010; Huang et al., 2018). Previous studies estimate that MCSs account for over half of the tropical precipitation (Yuan & Houze, 2010, hereafter referred as YH10), and in certain seasons over land regions the fraction can exceed 80% (Nesbitt et al., 2006; Roca et al., 2014).

Compared to most deep convective clouds, MCSs are of a larger horizontal scale and longer-lived, often persisting many hours with particularly long-lived storms lasting for more than a day. In addition to producing significantly larger volume of rainfall per storm, a key distinction of MCS is its large proportion of stratiform precipitation (Houze, 1997; Schumacher & Houze, 2003), resulting in a top heavier latent heating profile as opposed to a bottom heavy heating from convective precipitation (Schumacher et al., 2004; Liu et al., 2015). The top heavy heating profiles associated with tropical MCS have profound impact on the global circulation, extending beyond the tropics into midlatitudes (Schumacher et al., 2004).

MCSs are often embedded within various tropical waves such as convectively coupled Kelvin waves (Haertel & Kiladis, 2004), synoptic easterly waves (Schumacher & Houze, 2006), and the Madden-Julian Oscillation (MJO; Moncrieff, 2010). Tropical MCSs are thought to be an important building block for large-scale convective organizations such as the MJO due to its optimum upscale cascade effect for energy and momentum (Moncrieff, 2010). In midlatitudes, a type of strong MCS, known as mesoscale convective complexes (MCC; Maddox, 1980), tends to frequently occur within prominent baroclinic zones downstream of major mountain ranges such as the Rocky Mountains in the U.S., the Andes in South America, Ethiopian Highlands in Africa, and Tibetan Plateau in China (Laing & Fritsch, 1997, 2000).

MCSs in the U.S. have been extensively studied via weather satellites and the national weather radar network. Not only do MCSs contribute to comparable fractional total rainfall as those in the tropics, particularly in the Central U.S. (Fritsch et al., 1986; Feng et al., 2016; Feng et al., 2019; Haberlie & Ashley, 2019), but they also produce hazardous weather including flooding, large hail, tornadoes, and damaging winds (Doswell et al., 1996; Ashley & Mote, 2005; Smith et al., 2012; Stevenson & Schumacher, 2014). Regional studies have documented the characteristics of MCSs in China (Yang et al., 2015; Chen et al., 2019), central and south America (Machado et al., 1998), west Africa (Klein et al., 2018) and Europe (Morel & Senesi, 2002).

Satellite observations make it possible to study MCSs at the global scale. Two distinct methods are generally used in previous global MCS studies. The first type makes use of geostationary satellite data to track the evolution of MCSs based on their low cloud-top brightness temperature signatures in successive images (Laing & Fritsch, 1997; Roca et al., 2014; Huang et al., 2018). The second type is based on low-orbit satellite data, where advanced instrumentations such as spaceborne radar and microwave radiometers provide additional

This article is protected by copyright. All rights reserved.

measurements of cloud and precipitation structures, to characterize MCSs (Nesbitt et al., 2006; YH10; Liu & Zipser, 2013).

There are advantages and drawbacks for both methods. Geostationary satellite data can capture the entire lifecycle evolution of MCSs, including their initiation, upscale growth, and mature and decay phases (e.g., Machado et al., 1998; Roca et al., 2017; Feng et al., 2019). The lifetime, propagation speed, growth rate of MCSs can also be obtained to better understand their evolution. However, geostationary satellite data usually lack information on the detailed internal structure of convection such as precipitation and vertical structures. Low-orbit satellite data, on the other hand, can provide richer information such as 3D convective/stratiform features (Liu & Zipser, 2013; Houze et al., 2015), precipitating and non-precipitating cloud characteristics (Nesbitt et al., 2006; YH10), and estimates of latent heating profiles (Tao et al., 2006; Shige et al., 2007). But low-orbit satellite data have long revisit intervals and therefore lack temporal continuity. The "snapshot" nature of low-orbit satellite data necessitates the use of size and/or intensity of large precipitation features alone to characterize MCSs without considering their lifetimes, which is a key distinction between MCS and regular deep convection.

The two fundamentally different approaches in documenting global MCS distributions result in discrepancies. For example, comparisons of collocated observations from convective features observed by the Global Precipitation Measurement (GPM) Dual-frequency Precipitation Radar (DPR) and an MCS tracking database incorporating ground-based radar network data over the U.S. show that only ~70% of the GPM detected mesoscale convective features coincide with tracked MCSs (Wang et al., 2019), suggesting that using low-orbit satellite data without considering temporal evolution could overestimate MCS frequency and rainfall contributions. Previous works that combine geostationary satellite and low-orbit/ground-based platforms (e.g., Futyan & Del Genio, 2007; Feng et al., 2019) provide a more comprehensive approach to examine the lifecycle evolution and vertical structure of MCSs, but they are limited to certain regions and would require significant effort to be conducted globally over long time periods.

Past studies that use geostationary satellite data for tracking MCSs globally are mostly limited to the tropics (e.g., Roca et al., 2014; Huang et al., 2018), although MCSs are also commonly observed in midlatitudes (Laing & Fritsch, 1997; Machado et al., 1998; Wang et al., 2019). Tracking of MCSs using geostationary satellite infrared (IR) brightness temperature (T_b) in previous studies is based on the assumption that any long-lived (greater than several hours) cold cloud system (CCS) that reaches mesoscale dimensions is an MCS. This assumption is especially problematic in midlatitudes, because synoptic systems such as extratropical cyclones and frontal systems can also produce large CCSs, but they may not be associated with convection or even precipitation (Feng et al., 2019). The lack of global MCS studies that cover both the tropics and midlatitudes limits our understanding of the global distribution and the importance of MCSs in various geographic regions, as well as our ability to evaluate emerging high-resolution weather and climate models that can potentially simulate MCSs across the globe.

The recent availability of two long term high-resolution global satellite datasets presents an opportunity to address this gap. The NASA merged geostationary satellite T_b data (Janowiak et al., 2017) and the GPM Integrated Multi-satellitE Retrievals (IMERG; Huffman, Stocker, et al., 2019) precipitation data V06 (Tan et al., 2019a) have been made publicly accessible. The two global datasets combined provide half-hourly and 0.1° resolution between 60°S and 60°N for 20 years. The IMERG dataset has been demonstrated to provide consistent precipitation retrievals to resolve the diurnal cycle comparable to that derived from ground-based radar observations (Tan

This article is protected by copyright. All rights reserved.

Accepted Article

et al., 2019a). The goal of this study is to develop a new approach combining these two high-resolution satellite datasets to track MCSs globally for both tropics and midlatitude, to evaluate the satellite-tracked MCSs against available ground-based radar observations, and present global MCS characteristics obtained by tracking them in this new high-resolution database.

This paper is organized as follows: section 2 describes the observation datasets used in the study; section 3 presents the MCS tracking methodology development and its evaluation; section 4 discusses the application of the methodology to the global datasets and demonstrate the advancement of our new method compared to previous IR-only tracking methods; results of global MCS characteristics are provided in section 5; summary and conclusions are given in section 6.

2 Observational datasets

2.1 Satellite data for global MCS tracking

The two global high-resolution satellite datasets used in this study to track MCSs globally (60°S – 60°N) are the NASA Global Merged IR V1 infrared brightness temperature (T_b) data (Janowiak et al., 2017) and the GPM IMERG V06B precipitation data (Tan et al., 2019a). Both datasets are available from 1 June 2000 to 31 March 2020 as of the writing of this manuscript.

The merged geostationary satellite T_b dataset combines all available operational geostationary satellite data and includes viewing angle and parallax corrections. It provides continuous global coverage from 60°S – 60°N with a horizontal resolution of about 4 km and a temporal resolution of 30 min. The hourly T_b data (using the images at 30 min past the hour) is used to identify and track deep convective clouds associated with MCS similar to our previous studies (Feng et al., 2018; Feng et al., 2019). The NASA Global Merged IR T_b dataset does not perform intercalibration among different geostationary satellite sensors, which could cause some differences among regions covered by different satellites. As demonstrated by Fiolleau et al. (2020), more work is needed to homogenize the global IR T_b datasets collected from the fleet of multiagency meteorological geostationary satellites, especially for studying convective clouds with cold IR T_b. More detailed discussions on the impact of uncertainties in the IR T_b dataset on MCS tracking are provided in Section 5.1.

The GPM IMERG V06B precipitation data is a unified precipitation retrieval dataset from a network of partner satellites in the GPM constellation (Huffman, Bolvin, Braithwaite, et al., 2019; Huffman, Bolvin, Nelkin, et al., 2019; Huffman, Stocker, et al., 2019). The primary precipitation estimates in IMERG are from passive microwave (PMW) sensors using the Goddard Profiling algorithm (Kummerow et al., 2001; Kummerow et al., 2011; Kummerow et al., 2015). A quasi-Lagrangian interpolation scheme (i.e., morphing) is applied to the gridded PMW precipitation estimates to fill in the gaps between PMW overpasses using motion vectors derived from total precipitable water vapor from numerical models in V06 (Tan et al., 2019b).

The IMERG precipitation data used in this study is the "Final Precipitation L3 Half Hourly $0.1° \times 0.1°$ V06B" data (Huffman, Stocker, et al., 2019). To facilitate joint use of the T_b and IMERG precipitation data for MCS tracking, the 4 km T_b data is regridded to match the IMERG 0.1° grid using ESMPy, a Python interface to the Earth System Modeling Framework

This article is protected by copyright. All rights reserved.

(ESMF) regridding software (https://www.earthsystemcog.org/projects/esmpy/). While both the T_b and IMERG precipitation data are available at half hourly, we only use hourly data for MCS tracking to reduce the computational cost. Previous work in tracking MCSs using hourly data suggests such temporal resolution is sufficient for these large convective storms (Feng et al., 2019). A snapshot from one of the 30 min T_b data is used to represent convective clouds in an hour, and the two 30 min IMERG precipitation data are averaged to represent the hourly precipitation amount. After this preprocessing, a global T_b and IMERG precipitation data covering 60°S – 60°N at 0.1° × 0.1° and 1 hourly resolution is obtained for MCS tracking. In this study, we use 16 years of T_b and IMERG precipitation data (2001-2019, excluding 2003-2005, see Section 5.1 for details) to demonstrate our technique and examine the climatological characteristics of global MCSs.

2.2 Regional ground-based radar data for validation

Ground-based S-band weather radar data from the U.S. and China are used in this study to develop and validate the MCS tracking algorithm from satellite data. In the U.S., we use the recently developed 13-year (2004-2016) high-resolution (~4 km, 1 hourly) MCS database east of the Rocky Mountains (Feng, 2019) as the reference MCS dataset. The reference MCS database also uses the NASA Global Merged T_b data and synthesizes the Next-Generation Radar Network (NEXRAD) 3D mosaic radar reflectivity (Bowman & Homeyer, 2017) and the Stage IV radar-based precipitation estimates (Lin, 2011) with rain gauge bias correction. MCSs in this database are defined as a large CCS (T_b < 241 K) area exceeding 6×10^4 km^2, with a radar-defined precipitating feature (PF) of at least 100 km, containing convective feature radar reflectivity > 45 dBZ at any vertical level, and persisting for at least 6 hours. The Stage IV precipitation estimates are used to compare with the GPM IMERG precipitation data.

In China, a similar S-band ground-based operational radar network dataset over northern China is used. A 3D mosaic radar data has been generated by Chen et al. (2020) using the preprocessing module of the Advanced Regional Prediction System, which combines 21 individual radars to produce a gridded radar dataset with a 2 km horizontal and 500 m vertical resolution every 30 min. The China radar data used in this study is from 1 April 2016 to 13 July 2016. To identify MCSs consistently with those in the U.S., the China 3D mosaic radar data are regridded to match the 4 km NASA Global Merged T_b data following the same procedure used by Feng et al. (2019). Subsequently, the FLEXible object TRacKeR (FLEXTRKR) algorithm (Feng et al., 2019) is applied to the combined T_b and 3D reflectivity data at hourly resolution to track MCSs in China. This consistent radar data processing and MCS tracking framework facilitates comparison with the satellite data between the two different geographic regions.

3 Methodological development and evaluation

3.1 The global MCS tracking methodology

Most previous studies using automated tracking techniques to identify MCS regionally or globally only used geostationary satellite T_b data. When employing a tracking technique, an MCS is defined as a CCS that exceeds a certain area threshold continuously for some duration

This article is protected by copyright. All rights reserved.

(e.g., Machado et al., 1998; Jirak et al., 2003; Fiolleau & Roca, 2013; Huang et al., 2018). In this study, the FLEXTRKR algorithm (Feng et al., 2019) uses T_b primarily to track CCS, but we have developed a new approach that further incorporates precipitation characteristics associated with CCS to more accurately identify the MCSs. A similar method using collocated T_b and precipitation data from polar orbiting satellites has been used previously to develop an MCS climatology over the whole tropics (YH10). However, mesoscale tracking was not possible from polar orbit information, and therefore the YH10 method could only identify MCSs at their mature stage. Our method of tracking the time dependency of the collocated T_b and precipitation signatures associated with MCSs takes into account the whole lifecycle of MCSs. In addition, by applying the method to a wider range of latitudes we extend the MCS climatology globally to allow comparison of midlatitude and tropical MCS behavior.

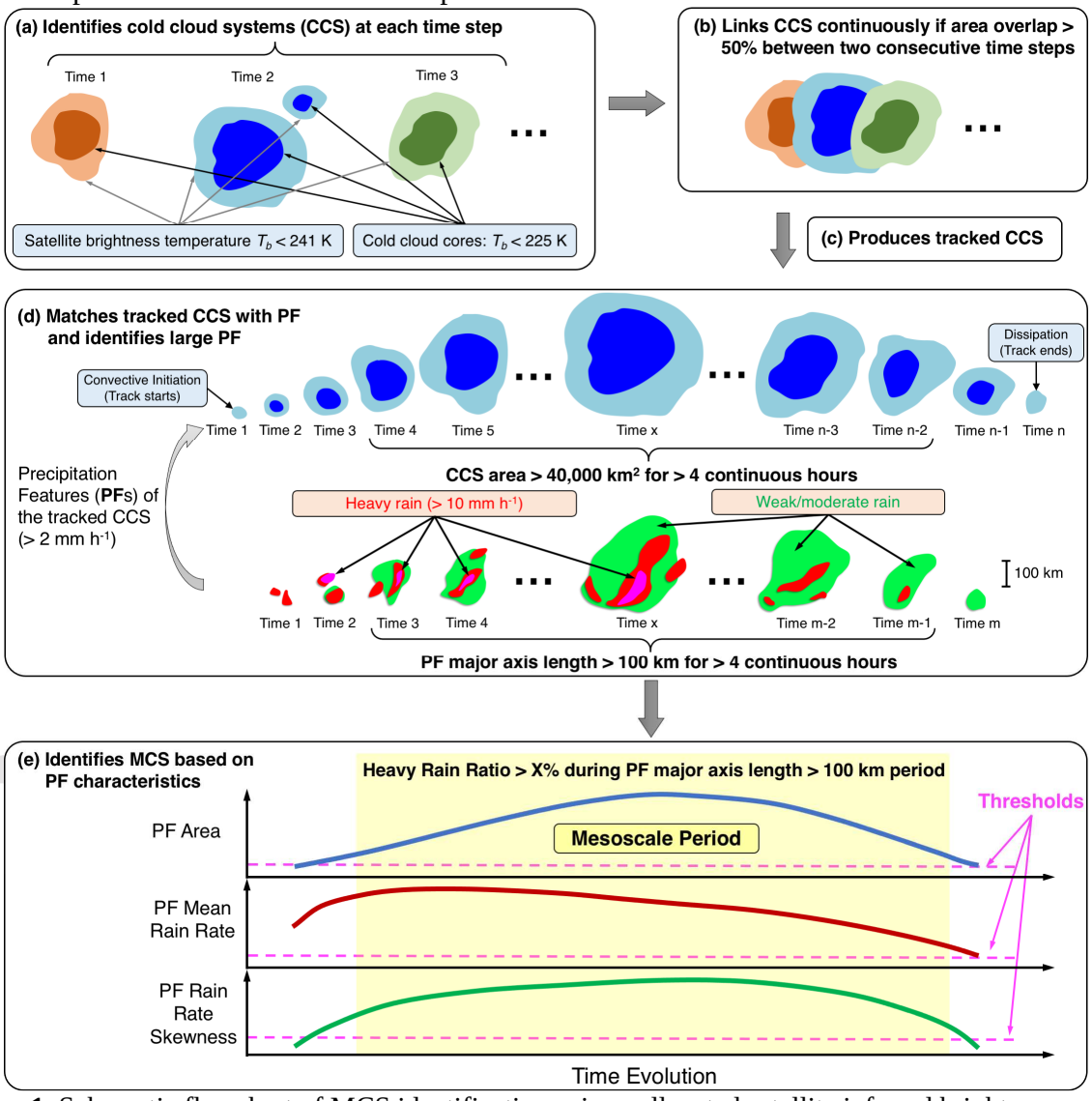

Figure 1. Schematic flowchart of MCS identification using collocated satellite infrared brightness temperature (T_b) and precipitation observations in this study. (a) Identification of cold cloud system (CCS) based on T_b signatures, (b) tracking of CCS between two consecutive times, (c) linking all consecutive times to produce tracks, (d) matches tracked CCS with associated precipitation feature (PF), and (e) identification of MCS based on PF characteristics. The yellow shading in (e) denotes the

This article is protected by copyright. All rights reserved.

mesoscale period as defined by CCS > 40,000 km^2, with a PF major axis length larger than 100 km for longer than 4 continuous hours. During this period, the PF area, mean rain rate and rain rate skewness must exceed the thresholds denoted by the magenta dash lines, and the heavy rain volume ratio during this period must be larger than X% (a function of lifetime, see **Figure 3d**) to qualify as an MCS. See text for more details.

In this study, we define an MCS as a convective system with:

1) CCS > 4×10^4 km^2 containing a PF with major axis length > 100 km,
2) PF area, mean rain rate, rain rate skewness and heavy rain volume ratio larger than corresponding lifetime dependent thresholds,
3) Both 1) and 2) last continuously for longer than 4 hours.

Figure 1 shows a schematic flowchart of MCS identification developed in this study which is explained in detail as follows.

Tracking convective systems using satellite T_b data typically starts with defining a CCS associated with deep convection. In the FLEXTRKR algorithm, a "detect and spread" approach to identify CCS has been implemented (Feng et al., 2018). As illustrated in **Figure 1 a**, cold cloud cores (T_b < 225 K) are first identified and labeled. They are then spread out iteratively to reach a secondary T_b threshold < 241 K to define a CCS. The iterative procedure starts from the largest cold cloud core in a given scene, spreading it by one pixel at a time outward surrounding the cold core to reach warmer T_b, followed by the second largest cold core, and so on. This procedure is based on the assumption that larger (mature) cold cloud cores have more time to detrain and form upper-level anvil clouds around them than smaller (young) clouds. Spreading of adjacent CCSs stops when the cloud boundaries of the CCSs touch each other. The iterative procedure ends when no cold cores in a scene can be spread within areas of T_b < 241 K. The remaining cold clouds (T_b < 241 K) with no cold cores that have not been identified are labeled if the cold cloud pixels form a contiguous area of > 800 km^2.

An update to use a coherent PF to connect multiple CCSs that share the same PF (Feng et al., 2019) has been implemented for precipitation data in this study. A coherent PF is defined as a contiguous area with hourly rain rate > 3 mm h^{-1}, whereas in previous work a PF was defined using low-level radar reflectivity data. The rain rate threshold, while admittedly arbitrary, is meant to retain contiguous areas of significant precipitation to assist in defining a coherent precipitating convective system for tracking. The precipitation field is first smoothed using a moving window (~30 km × 30 km) to reduce the noisiness of the hourly precipitation data. This "PF-assisted CCS definition" feature takes advantage of both the relative smoothness of the T_b field and the important PF associated with convection to identify individual CCSs, and better preserves coherent PFs during major precipitating stages of the MCS lifecycle to improve tracking fidelity and estimation of various storm statistics such as PF area in subsequent tracking steps.

The FLEXTRKR tracking of features in time uses a simple area overlap method. CCSs with an area overlap of more than 50% between two consecutive hours are linked as the same CCS (**Figure 1 b**). Tracking terminates when no other CCSs can be linked to the track. FLEXTRKR handles the track merging/splitting explicitly. When more than one CCS at time *n* are linked with one CCS at time *n*+1, tracking of the largest CCS at time *n* continues at time *n*+1,

This article is protected by copyright. All rights reserved.

Accepted Article

and the smaller CCSs at time *n* are flagged as merging and their trackings are terminated. Splitting of tracks is handled in a similar way, where the largest overlapping CCS at time *n*+1 is a continuation from the track at time *n*, but smaller overlapping CCSs are treated as newly generated tracks. The merge/split tracks are recorded such that they can be linked in the subsequent step.

Among all the tracked CCSs, a candidate MCS is defined as CCS area > 40,000 km^2 for longer than 4 continuous hours (**Figure 1 d**). The duration criterion is an important aspect of MCS because longer-lived MCSs not only produce 2-3 times the amount of rainfall compared to short-lived ones, but they also develop more robust stratiform precipitation and top-heavier diabatic heating profiles, thus exhibiting much stronger dynamical feedback to the large-scale environments through quasi-balanced mesoscale convective vortices (Yang et al., 2017; Feng et al., 2018). After identifying MCS candidates, non-MCS tracks with duration ≤ 12 hours are included as part of an MCS if they are mergers or splits of the MCS candidates. Manual examinations of the automated tracking results suggest including smaller mergers/splits often improves the tracking fidelity by correcting occasional over-segmentation of clouds during the CCS identification step. Such over-segmentation usually occurs in the decaying stage of MCS when cloud-top heights are decreasing at variable rates, as reflected by unevenly increasing T_b within tracked CCS.

The next step is to identify robust MCS from MCS candidates based on their PF characteristics. At a given hour, the PFs associated with an MCS candidate are defined as contiguous areas within the MCS with hourly rain rate > 2 mm h^{-1}. We determine the rain rate threshold by evaluating the global MCS tracking results with the U.S. NEXRAD MCS database described in Section 3.2. A suite of PF characteristics is calculated for each PF, including major axis length, area, mean rain rate, rain rate skewness, total rainfall volume, heavy rainfall (rain rate > 10 mm h^{-1}) volume, etc. The PF characteristics are used in the final step to determine if an MCS candidate can be identified as an MCS. For each MCS candidate, we define an "MCS period" as times when a PF major axis length > 100 km for > 4 continuous hours (**Figure 1 e**). This period denotes convection growing upscale to reach mesoscale dimension and produces major precipitation during the MCS lifecycle.

The conceptual evolution of an MCS viewed from its PF characteristics is shown in **Figure 1 e**. An MCS typically contains a large PF with high mean rain rate, especially during the upscale growth stage when most of the precipitation is convective, followed by a positive skewness of the rain rate distribution during the mature stage when mixed convective and stratiform rainfall coexist. During the "mesoscale period" (yellow shading in **Figure 1 e**), if the PF area, mean rain rate, and rain rate skewness, and heavy rain volume ratio (heavy rain volume/total rain volume) all exceed the lifetime-dependent thresholds, the MCS candidate is defined as an MCS. This approach is similar to our previous work in jointly using T_b and PF to identify MCS in mesoscale resolution (horizontal scale between 10-50 km) datasets (Feng et al., 2020). The PF area and mean rain rate criteria are designed to capture mesoscale PFs that have moderate-to-higher mean rainfall intensity, while the positive rain rate skewness (calculated from native pixel-level data) constrains the PFs to contain some intense convective-like precipitation (Feng et al., 2016). Our algorithm considers general mesoscale PF associated with MCSs, the definition of which has been evolving over the years (Houze et al., 1990; Houze, 2014; Houze, 2018). Compared to our previous work, one difference is the requirement of an additional criterion of the heavy rain volume ratio, which is designed to require that a fraction of the total

This article is protected by copyright. All rights reserved.

rainfall volume must be from convective precipitation (approximated by hourly rain rate > 10 mm h^{-1}). This is particularly relevant for midlatitude precipitation characteristics during the cold and/or transition seasons, when passages of baroclinic waves often produce persistent large CCSs, some of which can be associated with large PFs with moderate mean rain intensities, but the precipitation is stratiform in nature and consists of little convective/heavy precipitation (e.g., post-frontal rainbands in the cold sector) and hence should not be defined as MCSs. Nevertheless, the definition of MCSs in mid-and-high latitude rainbands, and/or atmospheric rivers (AR), especially over oceans, is a new use of the concept. Considering the nature of these mid-latitude weather systems, whether they should be defined as MCSs is ambiguous. Further work is needed to improve the understanding of such systems and whether the specific definition of MCS used in this paper should be refined. We discuss our approach in handling ambiguous mesoscale cloud systems in more detail in Section 4.1.

To determine the PF characteristics thresholds, we use the U.S. NEXRAD MCS tracking database from Feng et al. (2019) as a reference, which represents a more accurate identification of MCSs and their associated precipitation compared to the satellite T_b and IMERG precipitation datasets. In this analysis, data from the period of 2014-2016 between the NEXRAD MCS database and IMERG data are used. NEXRAD identified hourly MCS locations (~4 km resolution) are regridded to the IMERG precipitation grid (~10 km resolution). **Figure 2** shows an example of MCS in the U.S. Great Plains observed by the NEXRAD network, and the associated precipitation estimates from the Stage IV and IMERG dataset. The IMERG hourly PF morphology from this MCS is similar to that observed by NEXRAD radars (**Figure 2 a,b**), as the IMERG estimated PFs contain small regions of intense precipitation (rain rate > 10 mm h^{-1}) and broad regions of moderate-to-weak precipitation, in agreement with the expected distribution of convective and stratiform rainfall. The MCS event accumulated precipitation from IMERG generally agrees with that from Stage IV, albeit differences exist in detailed geographic locations receiving high rainfall amounts (**Figure 2 c,d**).

Accepted Article

This article is protected by copyright. All rights reserved.

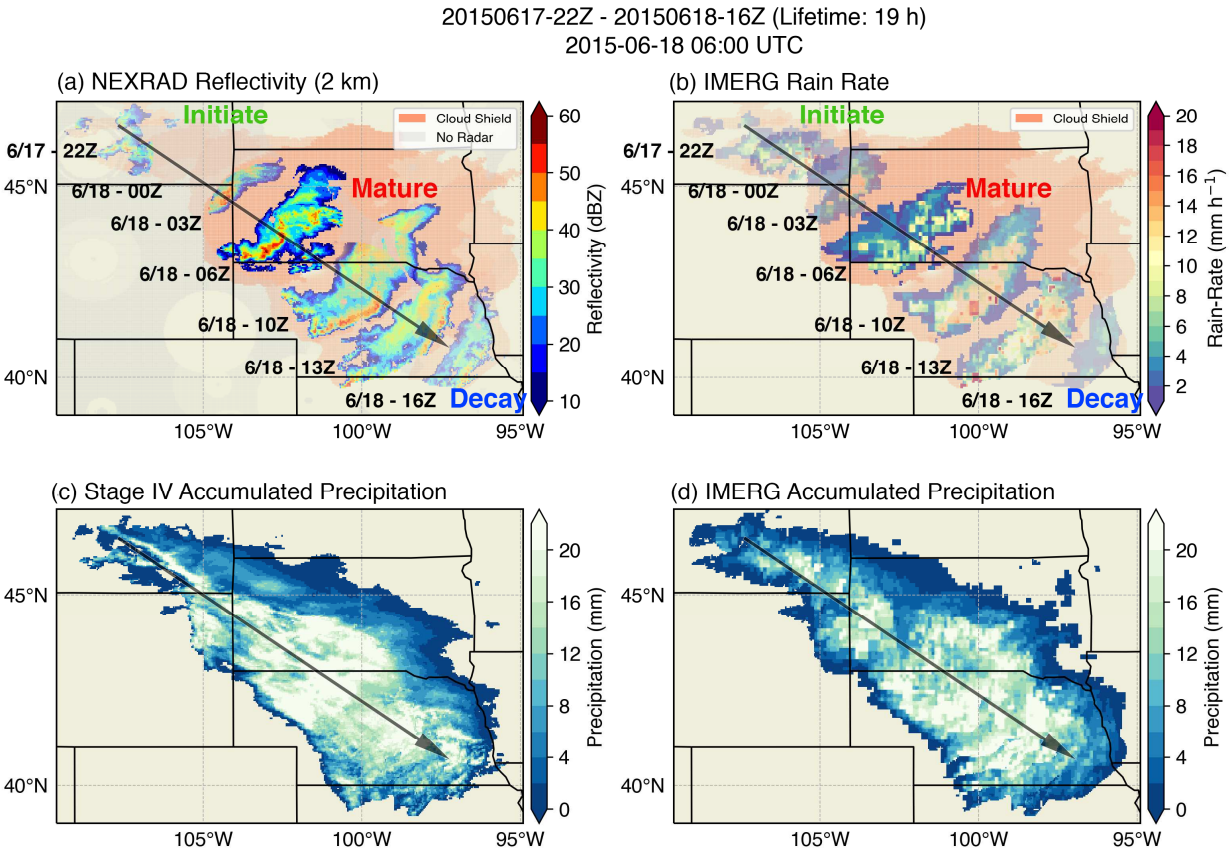

Figure 2. Example of a tracked MCS over the U.S. Great Plains depicted by NEXRAD radar network and GPM IMERG observations. (a) Snapshots of NEXRAD radar reflectivity at 2 km MSL during various MCS lifecycle stages, (b) similar to (a) except for IMERG instantaneous rain rate, (c) Stage IV accumulated precipitation for the tracked MCS, and (d) same as (c) except for IMERG accumulated precipitation.

The IMERG observed PF parametric characteristics within the NEXRAD-identified MCS locations during three warm seasons (March-October, 2014-2016) are shown as a function of MCS lifetime in **Figure 3**. It is clear that various PF parametric thresholds generally increase with MCS lifetime, suggesting that longer-lived MCSs typically have larger and more heavily precipitating PFs and larger rain rate skewness, denoting more convective-like precipitation. The linear fit lines in **Figure 3** represent various thresholds that can be used. Choosing higher PF parametric thresholds means only MCSs with larger and more intense PF are identified as MCSs, and vice versa.

This article is protected by copyright. All rights reserved.

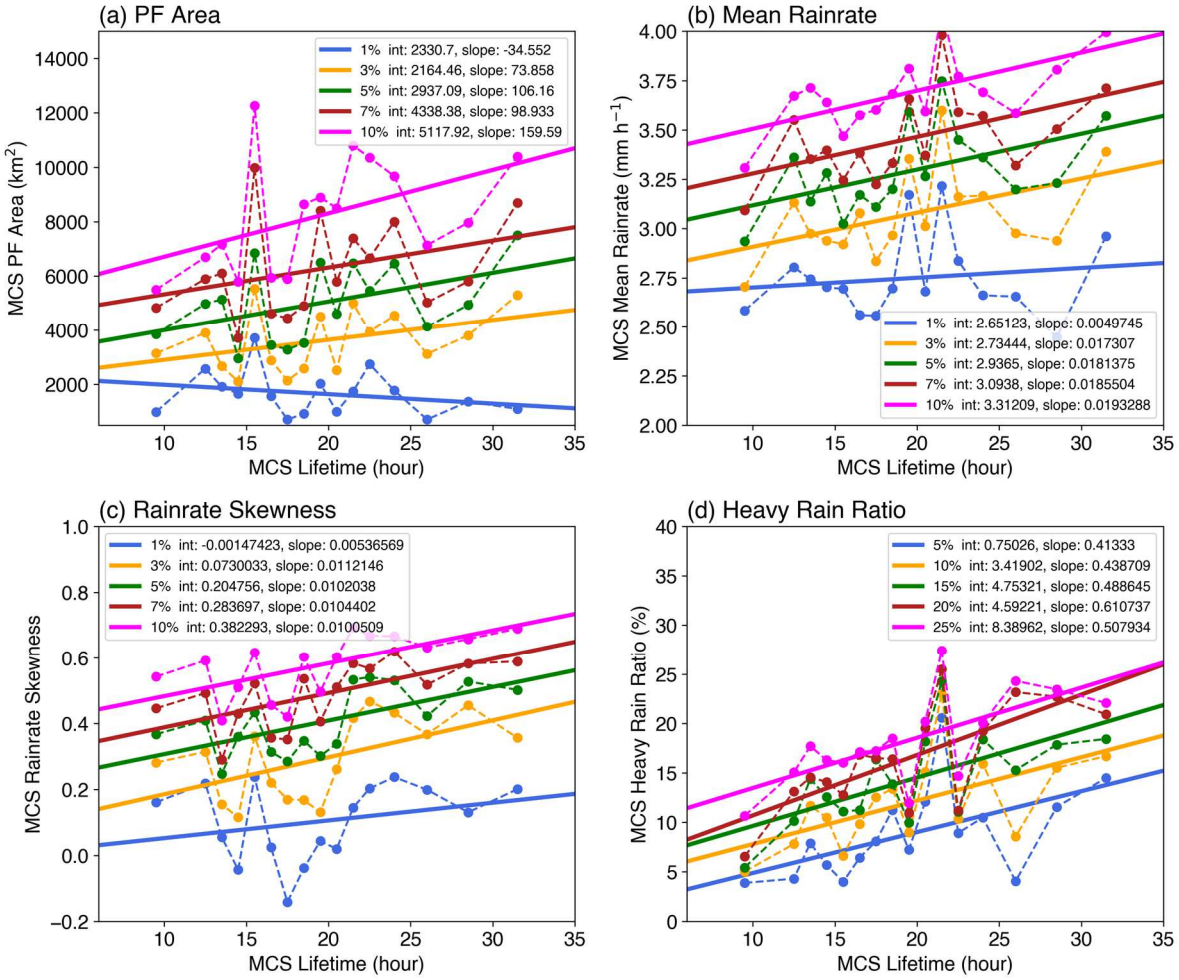

Figure 3. IMERG derived PF characteristics as a function of MCS lifetime. (a) PF area, (b) PF mean rain rate, (c) PF rain rate skewness, and (d) heavy rain volume ratio. Dots are specific percentile values shown in the legend, solid lines are linear fits to each set of percentile values. The fit intercepts and slopes are shown in the legends as well.

We use the NEXRAD MCS database to calibrate the PF parametric thresholds. By choosing increasingly lower thresholds (e.g., 10th, 5th, 3rd percentile fit lines), a larger population of MCSs is identified from the IMERG precipitation dataset. Through statistical comparisons with the NEXRAD MCS database, we determine the PF parametric thresholds that produce the best agreement in the number of MCS and the fraction of MCS precipitation to the total precipitation. These thresholds are the 5th percentile values for PF area, mean rain rate, rain rate skewness, and 10th percentile values for heavy rain volume ratio, respectively (thresholds given in the legends in **Figure 3**). For example, for an MCS that lasts 15 hours, the thresholds for PF area, mean rain rate, rain rate skewness and heavy rain ratios are approximately 4200 km^2, 3.2 mm h^{-1}, 0.3, and 10%, respectively. Calibrating these PF parametric thresholds against the NEXRAD-defined MCS database in the U.S. means the PF parameters are more tailored for mid-latitude continental MCS. However, such calibration should not affect detecting oceanic MCSs as our analysis results in Section 5 show that oceanic MCSs produce much heavier precipitation (both local rain rate and rainfall volume) than their land counterparts, making oceanic MCSs

This article is protected by copyright. All rights reserved.

Accepted Article

easier to exceed the PF parametric thresholds and captured by our method. We will validate the IMERG-based MCS tracking statistics against U.S. NEXRAD observations in Section 3.2, and further compare them with an operational radar network observations in northern China. Our efforts to validate the IMERG-based MCS data are limited by availability of radar network data in other regions.

3.2 Evaluation with the NEXRAD MCS database in the U.S.

The U.S. NEXRAD radar network provides the largest ground-based weather radar coverage in the world, which is excellent for evaluating the satellite coverage over this region and for calibrating the ability of the methodology for detecting midlatitude continental MCS. Comparisons of the spatial distribution of warm season (March – August) MCSs from the NEXRAD MCS database and the IMERG dataset during 2014-2016 are presented in **Figure 4**. In this comparison, the CCS area and duration thresholds for IMERG are adjusted to 60,000 km^2 and 6 hours to be consistent with that used in the NEXRAD MCS database (Feng et al., 2019). This means that only a subset of the longer-lived and more robust MCSs from the IMERG MCS tracking are included in the comparison, although including the shorter-lived and smaller MCSs only increase the MCS precipitation fraction by ~10% in this region.

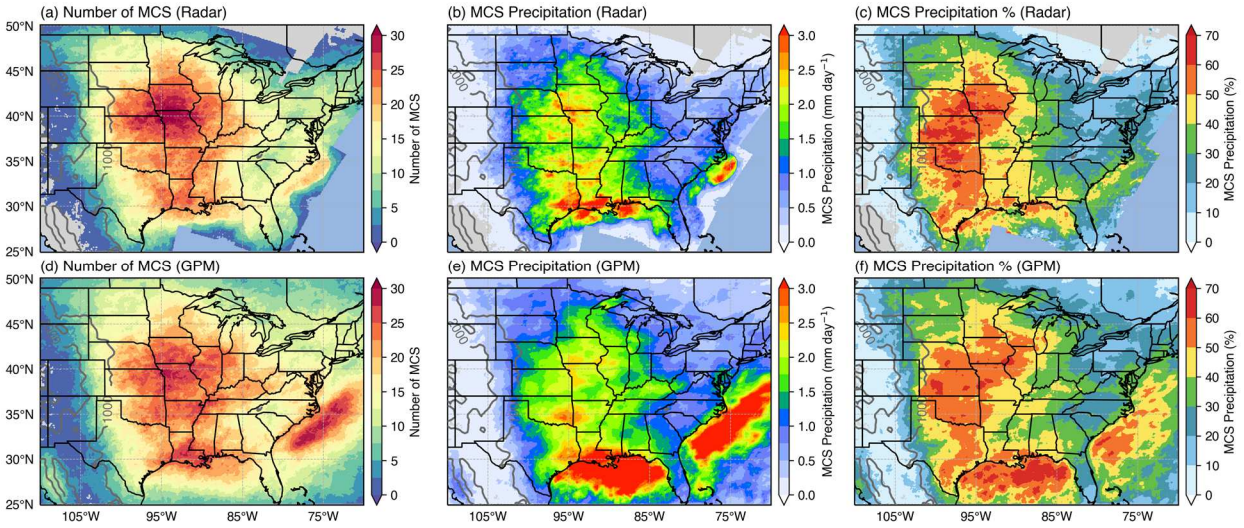

Figure 4. Comparison of the spatial distribution of observed warm season (March - August) MCSs tracked by NEXRAD radar dataset (top row) and GPM IMERG dataset (bottom row) for 2014-2016. (a,d) Number of MCSs, (b,e) MCS precipitation amount, and (c,f) MCS precipitation percentage to total precipitation. The number of MCSs in (a,d) is calculated by adding each swath of an MCS PF during its lifetime (counted as one sample over each grid point within the swath) over 3 warm seasons divided by the total number of seasons (3).

The comparison results show a good agreement between the IMERG-based MCS dataset and the NEXRAD MCS database over the continental U.S. The number of MCS passing over a given location and the average MCS precipitation amount both maximize in the middle of the Central U.S. (**Figure 4 a-b, d-e**), and the MCS precipitation fraction ranges between 40%-60% over the Great Plains and parts of the Midwest, with a consistent reduction in the Southeast and Eastern U.S. (**Figure 4 c,f**). Beyond the continental region, differences in the number of MCSs

This article is protected by copyright. All rights reserved.

and their associated precipitation increase with the distance from the coastal region, primarily as a result of the reduced NEXRAD radar coverage beyond the coastline. A secondary peak in MCS frequency occurs east of the Southeast coastline in the Atlantic where climatological sea surface temperature is high. While there is evidence of such enhancement in the NEXRAD MCS database, the IMERG MCS database shows MCS accounting for 40%-50% of the total rainfall in that region. This comparison highlights the advantage of the IMERG MCS database that provides complete coverage beyond ground-based radar asset regions.

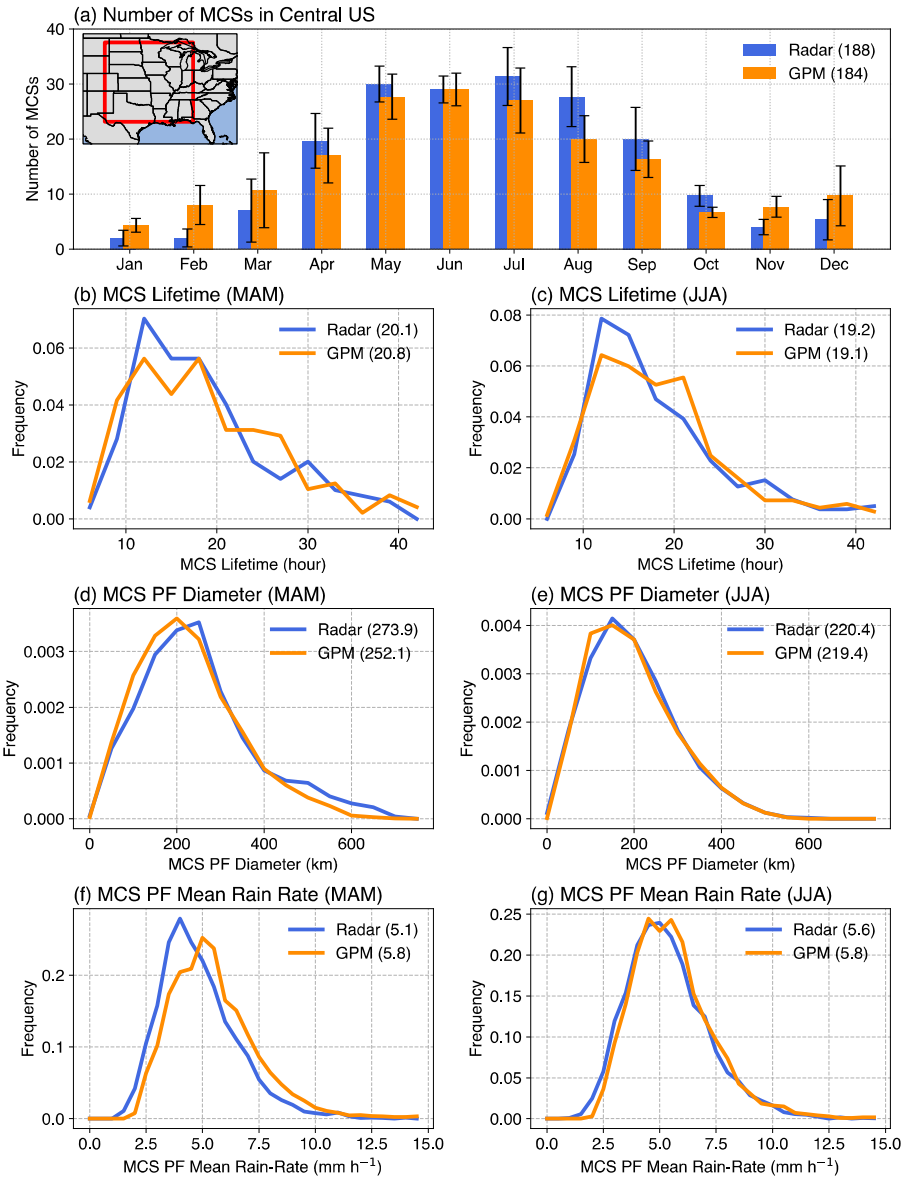

Figure 5. Comparison of MCS statistics over Central U.S. tracked by NEXRAD radar dataset and GPM IMERG dataset during 2014-2016. (a) Monthly average number of MCS (bars) and standard deviation (error bars), probability density function (PDF) of MCS properties are shown in (b-g) for MAM (left column) and JJA (right column), respectively. (b-c) MCS lifetime, (d-e) MCS PF diameter, (f-g) MCS PF mean rain rate. The region of comparison is shown as the red box in the inset of (a).

Detailed comparisons of the MCS seasonal cycle and PF characteristics in the Central U.S. are shown in **Figure 5**. The total annual mean number of MCS initiated within the Central

This article is protected by copyright. All rights reserved.

Accepted Article

U.S. is around 180 in both datasets. The monthly average number of MCS are also comparable between the two datasets (**Figure 5 a**), although the IMERG-based MCS numbers are slightly lower during the warm season (April – October) and slightly higher during the cold season (November – March). This bias suggests that some convectively intense MCSs identified by the NEXRAD radar data during the warm season may not satisfy the precipitation criteria from the IMERG precipitation data, while some heavily precipitating mesoscale cloud systems identified by IMERG data as MCSs during the cold season may not meet the radar-based convective intensity criteria (> 45 dBZ). Nevertheless, the distributions of the MCS PF characteristics from the IMERG-based MCS dataset, including the MCS PF lifetime, diameter and mean rain rate agree remarkably well with those from the NEXRAD MCS database, except the PF mean rain rate in spring from the IMERG-based dataset is slightly higher. These results are encouraging because the IMERG data is able to estimate important PF characteristics for a variety of PF sizes and intensities. As such, the IMERG data should be able to identify MCSs in other parts of the world where large-scale conditions might favor MCS with sizes and intensities are different than those in the U.S. We note that the above comparisons are sensitive to the rain rate threshold used to define a PF. As mentioned in Section 3.1, we use 2 mm h^{-1} as a threshold to define PF in the IMERG data, which is higher than that used in the NEXRAD Stage IV precipitation data (1 mm h^{-1}). This is because the IMERG data is found to overestimate areas with weak rainfall intensity in MCSs (Cui et al., 2020). Using slightly higher rain rate thresholds can mitigate the bias in estimating PF parameters in the U.S. We note that this choice of rain rate thresholds is likely product-dependent and that using a different satellite precipitation product may require different thresholds. The diurnal cycle of warm-season MCS vs. non-MCS precipitation from IMERG compares quite well with the NEXRAD MCS dataset (**Figure S1**), demonstrating the advantage of IMERG with a high temporal resolution.

3.3 Evaluation with weather radar observations in China

To assess the robustness of the IMERG-based MCS dataset in other geophysical regions, we compare the MCSs tracked with the IMERG data to those tracked with the 21 ground-based operational radar network data in northern China during 1 April – 13 July in 2016 (see descriptions in Section 2.2).

The IMERG-tracked MCS lifetime generally compares well with the radar-tracked data, although the IMERG-based dataset produces more longer-lived MCSs lasting beyond 15 hours (**Figure 6 a**). This could be partially attributed to the limited radar coverage in northern China. Some longer-lived MCSs that initiate inland continue to propagate eastward into the Yellow Sea (between mainland China and the Korean Peninsula). As they move beyond the range of the ground-based radar, PFs estimated from the ground-based radar become unavailable while they can still be detected from the IMERG data, causing some discrepancies in the long-lived MCS lifetime estimates between the two tracking datasets. The monthly number of MCSs also agrees well, with most of the MCSs in this region occurring in June (**Figure 6 b**). Comparisons of the time series of MCS detection show that most MCS events, particularly those with larger PFs, are consistently identified in both datasets (**Figure S2**).

The above evaluation results in two different geographic regions suggest that our new MCS tracking algorithm jointly using the geostationary satellite T_b and GPM IMERG precipitation data can provide consistent MCS tracking results with those obtained by using

This article is protected by copyright. All rights reserved.

Accepted Article

ground-based radar data. Despite these encouraging agreements, we emphasize that satellite-based precipitation retrievals such as GPM IMERG used in this study are not a replacement of surface radar network in providing high spatiotemporal resolution depiction of convective cloud systems. Radar observations provide important 3D characteristics of MCSs, allowing separation of convective and stratiform regions that have distinctive precipitation and latent heating characteristics that cannot be obtained from IMERG precipitation data. Further, both evaluations described above are conducted in midlatitude continental regions based on the radar data available to us, future work should further validate IMERG data in other geographic regions, particularly over tropical oceans. Considering no ground-based radar exists over majority of the ocean except limited island locations, such validation will likely rely more on comparisons with other satellite observations such as the GPM DPR, the Tropical Rainfall Measuring Mission (TRMM) Precipitation Radar, or the A-Train satellites (Stephens et al., 2002). Some comparisons between our results with past studies are discussed in Section 5. Nevertheless, the evaluations presented above show that our technique based on IMERG data over land captures MCSs of a variety of sizes and intensities, giving us more confidence that our method will produce reasonable MCS tracking results over remote tropical regions.

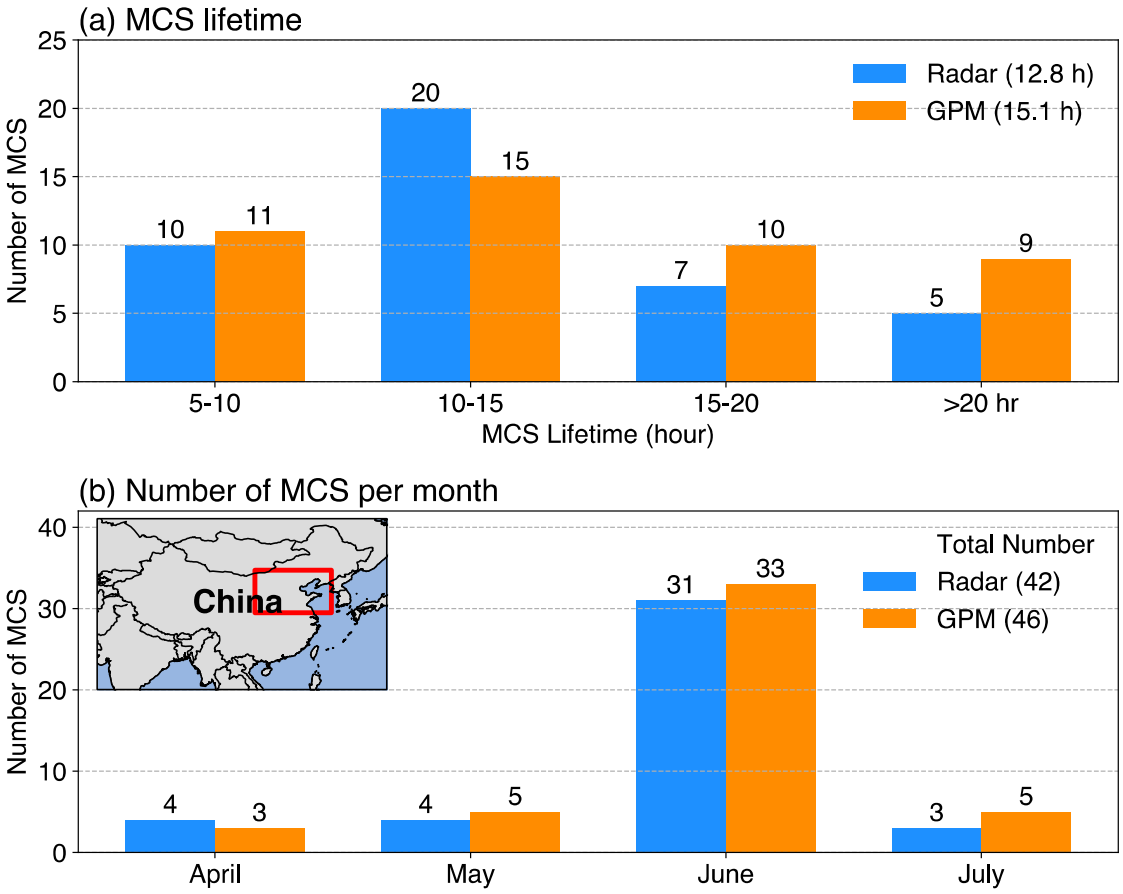

Figure 6. Comparisons of MCSs over northeastern China tracked by using ground-based radar network data and GPM IMERG data during 2016. (a) Distribution of MCS lifetime, and (b) number of MCSs per month. The region of comparison is shown as the red box in the inset of (b).

This article is protected by copyright. All rights reserved.

4 Application to global satellite data

4.1 Exclusion of TC and AR in MCS tracking dataset

The global merged T_b and IMERG precipitation data covering 60°S – 60°N with 0.1° × 0.1° spatial and hourly temporal resolution consist of 3600 × 1800 pixels and 8760 frames per year. Running the MCS tracking algorithm on the entire globe at the same time is possible, but not computationally efficient for developing a long-term dataset. Therefore we divide the Earth into three regions (**Figure S3**) to conduct the MCS tracking on each region separately: Asia-Pacific (35°E – 180°E, 60°S – 60°N), Europe-North America (180°W – 50°E, 20°N – 60°N), and Africa-South America (180°W – 50°E, 60°S – 30°N). These three regions are large enough to contain most MCSs with minimal impact from those MCSs crossing from one region to another. The overlapping areas between the three regions further allow a "buffer zone" to reduce discontinuity when the regional data are stitched together to develop the global data. Tracking is run continuously from 1 January to 31 December of each year for each region to minimize the impact of artificial termination of MCSs that span two different tracking periods.

Figure 7 shows an example of the MCS tracking results over the Maritime Continent (also see the included animation in the supplementary information). CCSs associated with the tracked MCSs are indicated by the magenta contours in **Figure 7 a** and the various color shadings on top of the GPM IMERG precipitation field in **Figure 7 b**. This example shows that most mesoscale PFs that produced heavy precipitation were associated with tracked MCSs. In addition, the detect-and-spread CCS identification technique in FLEXTRKR (Feng et al., 2018) is able to separate nearby MCSs that shared cold anvil cloud shields but have separate PFs (e.g., the two MCS clusters around 10°S, 125°E).

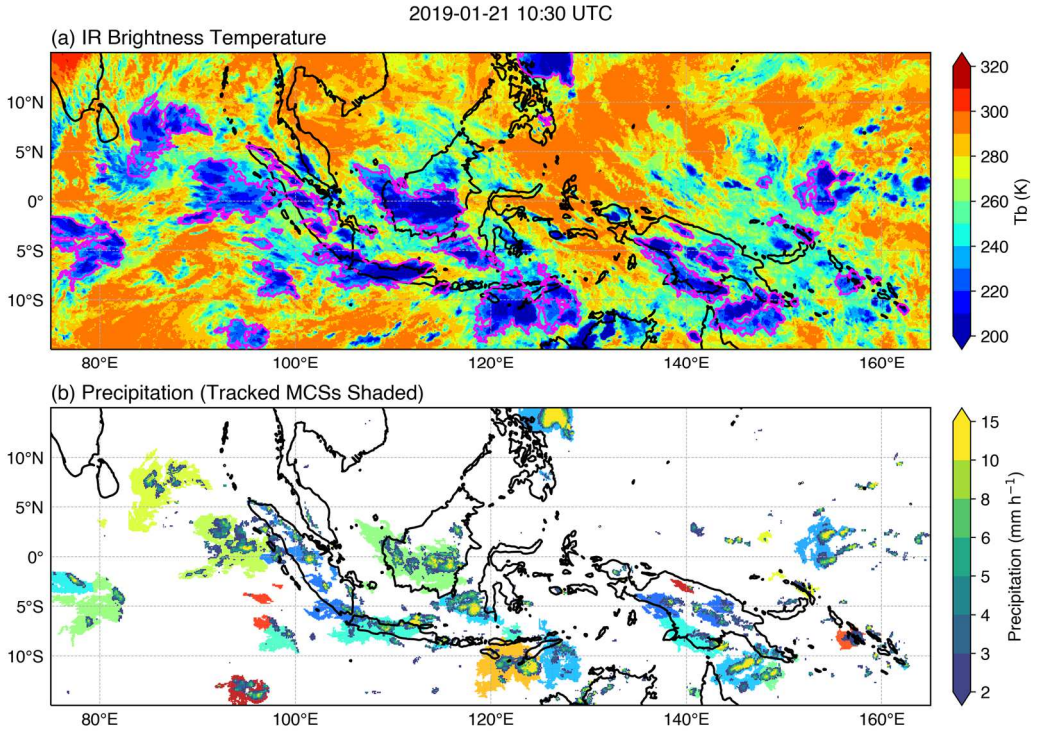

Figure 7. Example snapshot of tracked MCSs over the Maritime Continent at 10:30 UTC on 21 January 2019. (a) Infrared brightness temperature, (b) GPM IMERG precipitation. The magenta contours in (a) and the color shadings behind large clusters of PFs in (b) denote each tracked MCS. Weak rain rates < 2

This article is protected by copyright. All rights reserved.

mm h^{-1} in (b) are excluded for clarity. Animation for this day is provided in the supplementary information.

Since our MCS tracking only considers CCS with low T_b and mesoscale PF signatures, other large precipitating cloud systems that are not MCSs but exhibit similar characteristics could have been included as MCSs. The most obvious example is tropical cyclone (TC). Although TC bears similarity with MCS in both T_b and precipitation characteristics, their formation and maintenance mechanisms are different from MCS. To exclude TCs in our MCS tracking database, we use the International Best Track Archive for Climate Stewardship (IBTrACS) TC v4 database (Knapp et al., 2010; Knapp et al., 2018). The IBTrACS database contains global TC information at a minimum of 3 hourly resolution (certain regions contain higher temporal resolution). Each TC has a centroid location, time, and a series of TC characteristics such as the maximum wind speed, minimum pressure, etc. We use the estimated mean radius of the outermost closed isobar as the radius of a TC. When the radius of the last closed isobar is unavailable, the maximum radius of 30/34 kt wind among all four quadrants is used. This decision is made such that we exclude the potential influence of TC in our MCS database as much as possible. For MCSs in our tracking dataset, if the CCS mask (e.g., color shading areas in **Figure 7 b**) associated with a tracked MCS overlaps with the TC radius mask at any given time during the MCS lifetime, that MCS is excluded from our tracking database. This stringent requirement is designed to exclude any MCSs in the proximity of a TC.

In close examination of the geographic distribution of MCSs from our tracking database, we find two regions commonly affected by AR during the cool season (September – February) in the Northern Hemisphere, the North American West Coast and European West Coast (Rutz et al., 2019), showing higher numbers of MCSs identified than expected. This is likely due to orographic enhancement of precipitation when AR makes landfall in regions of complex terrain, and the high intensity PFs and the expansive frontal stratiform clouds are aliased as MCSs. As orographic enhancement during AR events in the cool season is often associated with seeder-feeder clouds (Creamean et al., 2013), such PFs should not be included as MCS, although MCSs have been found in associated with ARs during the warm season (Moore et al., 2012). To identify AR events, we use a high-resolution global AR dataset (Rutz et al., 2019) based on the tracking of ARs in the Modern-Era Retrospective Analysis for Research and Applications, Version 2 (MERRA-2) data. The AR dataset has hourly and $0.5° \times 0.625°$ (latitude $\times$ longitude) resolution. Similar to the procedure for excluding TCs, MCSs (using the CCS mask) that overlap with an AR are excluded from our database. We only exclude MCSs within landfalling ARs over the two West Coast regions with sigifinicant topography changes as defined by Rutz et al. (2019, Figure 4). This is because over the ocean, cyclone genesis and frontogenesis associated with AR often produce intense precipitation over a strengthening cold front. The vertical structure of convective and stratiform precipitation and associated latent heating generated by forced ascent in frontogenesis environment closely resemble MCS (Cannon et al., 2020). Therefore, MCSs in our database over the Northeastern Pacific and Northeastern Atlantic Oceans are retained even if they are within ARs. These heavily precipitating rainbands and mesoscale cloud systems in the midlatitudes, particularly those over the ocean, should be re-examined in future research to better understand their nature and to determine whether the definition of MCS used in this study should be refined.

This article is protected by copyright. All rights reserved.

The annual averaged numbers of excluded MCSs near TCs in Asia-Pacific, Europe-North America, and Africa-South America regions are 332, 202 and 83, respectively. These excluded MCSs only account for 1%-3% of the total MCS populations in each region. In contrast, the annual averaged number of excluded MCSs in landfalling ARs is 369, ~10% of the MCS populations in Europe-North America, suggesting that intense precipitation systems within landfalling ARs play a non-negligible role in the West Coast of North America and Europe. During the 16-year study period (2001-2019, excluding 2003-2005), the average number of MCS tracked in the globe is approximately 29,073 per year. Asia-Pacific and Africa-South America have a similar number of MCSs, averaging ~13,257 $year^{-1}$ and ~13,340 $year^{-1}$, respectively, while Europe-North America has ~2,476 $year^{-1}$. Separating by latitudes, the tropics (20°S – 20°N) has ~19,915 MCSs per year, followed by the Northern Hemisphere (20°N – 60°N) with ~4,952 $year^{-1}$, and the Southern Hemisphere (20°S – 60°S) with ~4,206 $year^{-1}$.

4.2 Comparison with previous IR-only method

Compared to previous IR-only MCS tracking methods (Laing & Fritsch, 1997; Roca et al., 2017; Huang et al., 2018), the key feature of the algorithm developed in this study is the use of precipitation characteristics in addition to IR signatures to identify MCSs. MCSs in the IR-only methods are commonly defined as a cloud system (a contiguous area with IR T_b below some temperature threshold values) larger than some area thresholds and persists for at least a few hours. This method has some validity in the tropics where most long-lived cloud systems with cold cloud tops reaching the mesoscale dimension are associated with MCSs. However, combining cloud-top temperature with precipitation observed by satellite produced a more accurate census of MCSs in the tropics (YH10). In this study we have further improved the approach by adding time-dependent tracking to the combination of T_b and precipitation. In midlatitudes, the IR-only method has been useful for MCSs during the warm season in the Americas (Fritsch et al., 1986; Machado et al., 1998; Jirak et al., 2003), China (Yang et al., 2015; Chen et al., 2019) and Europe (Morel & Senesi, 2002). Outside of summer when baroclinic forcing is much stronger in the midlatitudes, large and long-lived cloud systems viewed from IR data alone are often insufficient to identify MCS, as many synoptically-forced clouds not associated with MCS bear similarity with large and long-lived MCSs in IR signatures (i.e., large and long-lived).

To demonstrate the advance of our new algorithm compared to previous IR-only MCS tracking methods, we compare the MCS populations identified by IR-only method and our new IR+PF method over Asia. MCSs identified by the IR-only method are the "MCS candidates" that are described in Section 3. **Figure 8** shows the spatial distribution of the difference in seasonal mean number of MCS between the two methods. Over the tropics (south of 20°N) the largest difference is ~10% across all seasons, suggesting that most tracked mesoscale cloud systems in the tropics produce precipitation that satisfies our PF criteria calibrated from midlatitude MCSs (Section 3.1). It also means that our method should produce consistent MCS identification with previous IR-only methods over the tropics, facilitating comparison with previous studies. In contrast, in the midlatitude, particularly in non-summer seasons, significant differences in the number of MCSs are found over Central Asia, extending to the Northern Pacific Ocean during boreal spring (MAM) and winter (DJF). On average, the IR-only method identifies 30-50 more MCSs (a factor of 5-20) over the Tibetan Plateau and the Tian Shan mountain ranges in spring

This article is protected by copyright. All rights reserved.

Accepted Article

and winter. Even during boreal summer (June-August), the IR-only method still identifies a notably higher number of MCSs (15-20, or a factor of 2) over the Tibetan Plateau compared to the new IR+PF method.

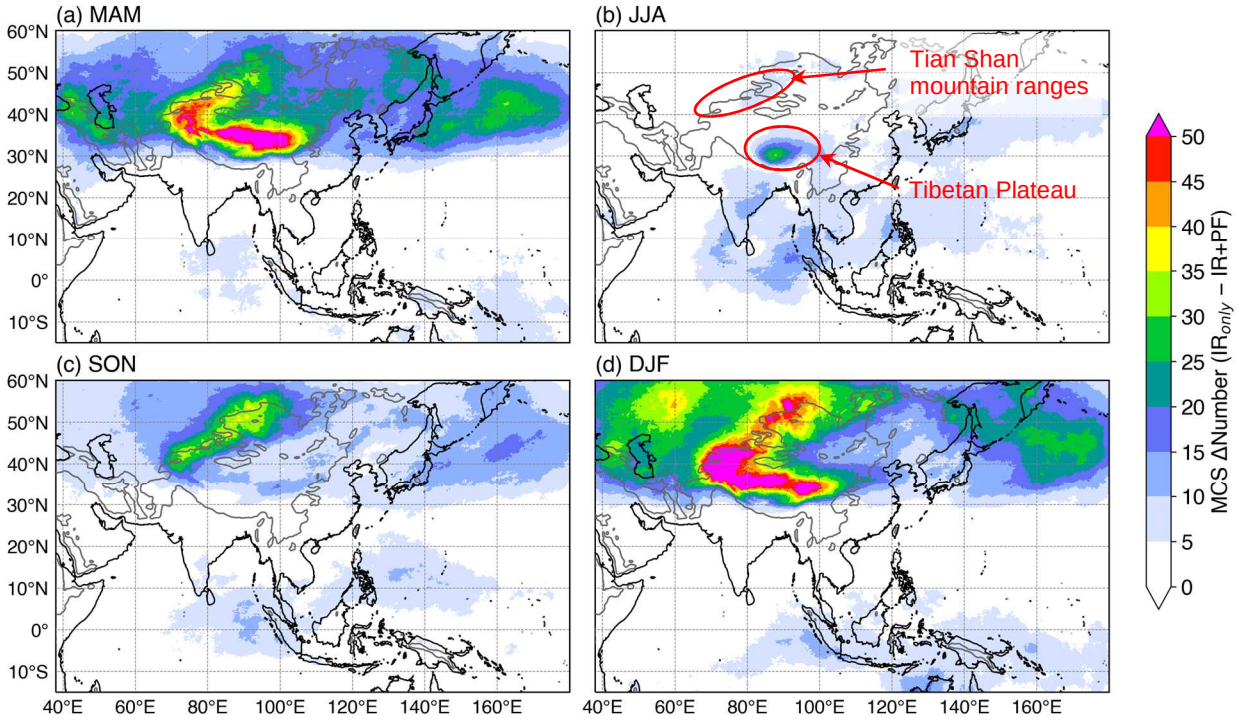

Figure 8. Spatial distribution of the average differences in the number of MCSs between IR-only method and the new robust MCS method in this study during the four seasons for 2014-2019. (a) March–May, (b) June–August, (c) September–November, and (d) December–February. Gray outlines in the background are terrain elevations higher than 1000 m.

To help explain the discrepancy between the IR-only and IR+PF methods, we compare four PF characteristics associated with MCS populations identified between the two methods. **Figure 9** shows the joint probability density functions (PDF) of Central Asian (28°N – 60°N, 50°E – 120°E) MCS lifetimes and the four PF characteristics that are used to define MCS in this study (see Section 3.1), namely PF area, PF mean rain rate, rain rate skewness, and heavy rain ratio. Results show that a large fraction of MCS defined by the IR-only method have PF area and PF mean rain rate below their respective thresholds used in the IR+PF algorithm, followed by a smaller fraction that fails the rain rate skewness and heavy rain ratio criteria. This finding suggests that many tracked long-lived large CCSs in the IR-only method contain very small PFs with low rainfall intensity and sometimes stratiform-like precipitation (weak spatial variability as suggested by low skewness, and low fraction of heavy rainfall), inconsistent with MCS characteristics. A typical example of large tracked CCS with scattered weak precipitation over the Tibetan Plateau is shown in **Figure S4**. Similar joint-PDF analysis for summer season MCS populations further finds that tracked convection from the IR-only method often has too small PF areas, although mostly satisfying the other three PF criteria (not shown). The PF area thresholds used in our algorithm are not particularly high. For example, for a system with 5-hour lifetime, the PF area threshold (**Figure 3 a**) is 3467 km^2, or 66 km equivalent diameter. Systems failing to exceed this PF area threshold should not be identified as MCSs.

This article is protected by copyright. All rights reserved.

Accepted Article

Accepted Article

These analyses, while only conducted over Asia, demonstrate that our new MCS tracking algorithm that considers key PF characteristics in identifying MCSs is more accurate than previous IR-only MCS tracking algorithms over the midlatitudes, particularly in non-summer seasons. This new algorithm can be applied globally for both the tropics and midlatitudes over all seasons to develop a global MCS tracking database.

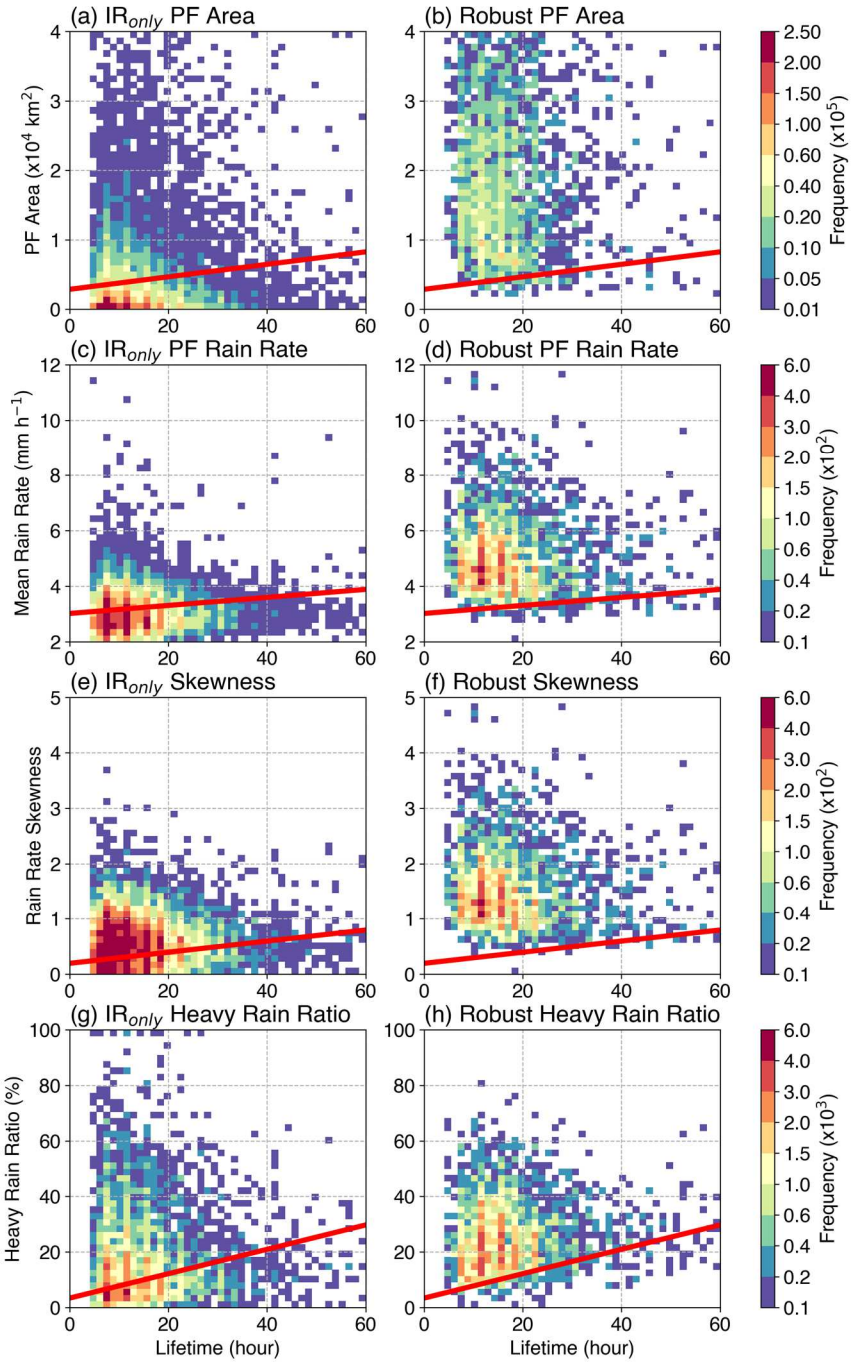

Figure 9. Comparisons of the joint PDF of PF parameters between MCSs defined by IR-only method (left column) and the new IR+PF method (right column) over Central Asia region (28°N – 60°N, 50°E – 120°E) for all seasons during 2014-2019. (a-b) PF area, (c-d) PF mean rain rate, (e-f), PF rain rate

This article is protected by copyright. All rights reserved.

skewness, and (g-h) heavy rain ratio. Red lines denote thresholds used to define robust MCSs for each PF parameter. The MCS lifetime here is defined by the tracked CCS duration. Mean values of the PF parameters throughout each MCS lifetime is used.

5 Global MCS characteristics

5.1 MCS frequency and precipitation

Global distributions of the annual mean number of MCSs, MCS precipitation amount, and MCS contribution to annual total precipitation during the 16-year period (2001 – 2019, excluding 2003-2005) are shown in **Figure 10**. The number of MCSs is calculated by counting the entire swath of precipitation at the 0.1° × 0.1° pixel associated with a tracked MCS once, then summing up the count for all observed MCSs. The annual mean number of MCSs at a given 0.1° × 0.1° pixel refers to the number of MCSs passing over that pixel per year. MCS precipitation amount is calculated by averaging all precipitation within the MCS cloud mask (i.e., CCS).

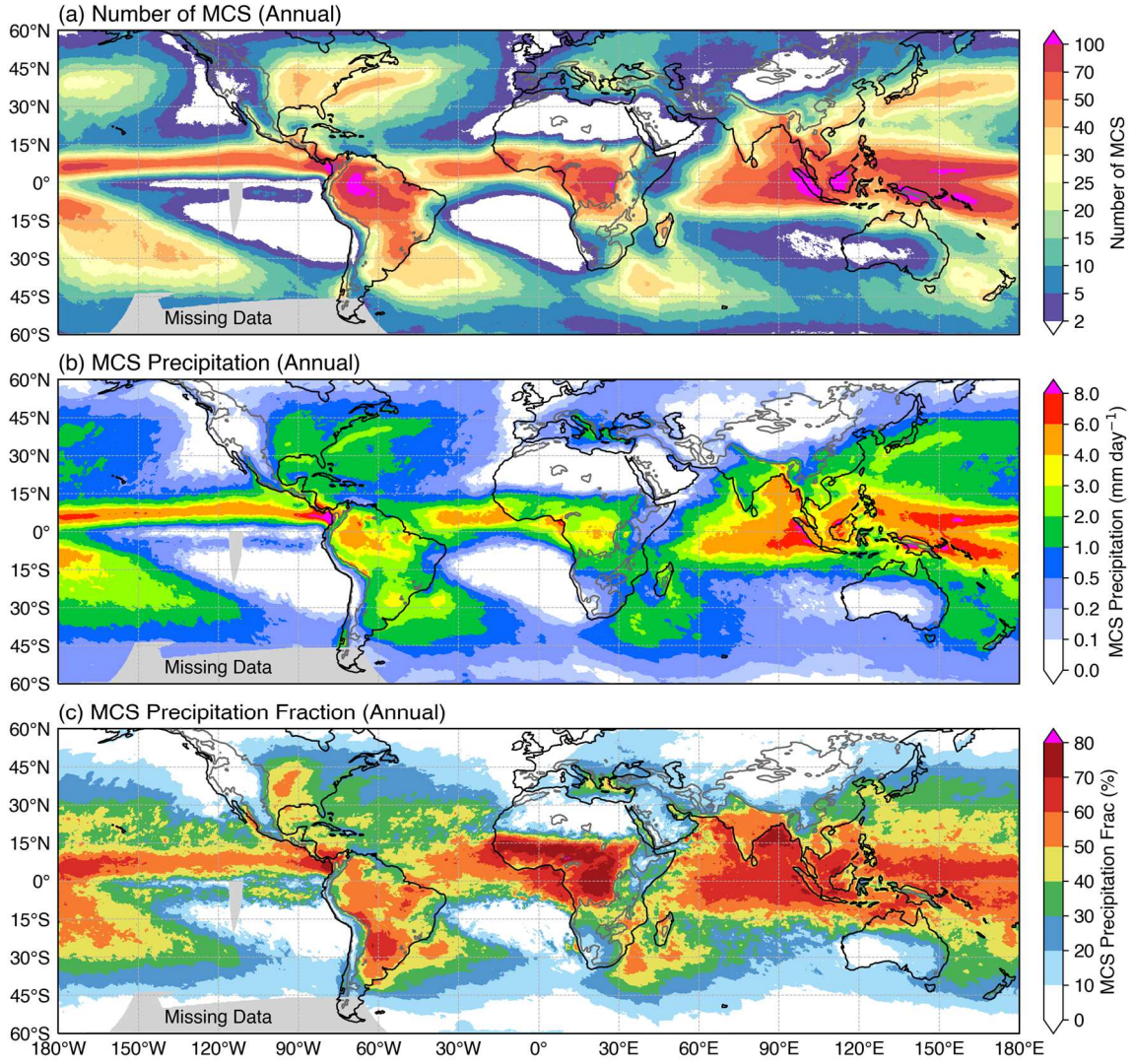

Figure 10. Annual mean global distribution of (a) the number of MCS, (b) MCS precipitation amount, and (c) percentage of MCS precipitation to total precipitation between 2001-2019. Dark gray contours

This article is protected by copyright. All rights reserved.

show terrains higher than 1000 m. The gray shaded regions over the Southern Pacific Ocean have frequent (> 25%) missing T_b data that affects MCS tracking and is therefore masked out.

MCSs occur both in the tropics and midlatitudes (**Figure 10 a**). The deep tropics (within 20°S – 20°N) have the largest number of MCSs, particularly over the Indo-Pacific warm pool, Central Africa, the Amazon, and tropical Eastern Pacific, averaging over 70 MCSs per year over broad regions. The geographic distribution of tropical MCSs found in this study is broadly consistent with previous MCS climatology studies (YH10 Fig. 9; e.g., Huang et al., 2018 Fig. 4). Huang et al. (2018) used IR T_b only to track MCSs in the tropics, while YH10 used joint T_b and precipitation signature similar to this study to identify mature MCSs except without tracking. The consistency between our results with these past studies that use different methodology lend further credence to the application of our current method over the whole Earth, even though the PF parameters were more tailored for midlatitude continental MCSs (Section 3.1). In the midlatitudes, the Central U.S., Argentina, Eastern China and Central Europe, are the major continental regions that favor MCS developments. Over ocean, MCSs are also frequently observed offshore of the east coast of North America, South America, East Asia, and South Africa, where influence of warm ocean currents, gravity wave generation, synoptic disturbances, flow over mountain ranges, or some combination of these factors affect MCS occurrence.

The distribution of MCS precipitation amount largely follows the MCS density (**Figure 10 b**), with the largest annual mean MCS precipitation amount found over tropical Eastern Pacific offshore from the Columbian coast, Indo-Pacific warm pool west of Sumatra and surrounding oceans near the Solomon Islands. MCS contribution to annual total precipitation exceeds 50% across the majority of the tropical belt (15°S – 15°N), with several ocean basins reaching above 60%, including the Indo-Pacific warm pool, Bay of Bengal, tropical Eastern Atlantic, and tropical Eastern Pacific (**Figure 10 c**). Using a similar combination of T_b and precipitation data, YH10 also found that mature MCSs account for 56% of total tropical rainfall, consistent with our results. Over continents, the most notable region with the highest MCS rainfall fraction is the West African Monsoon region, exceeding 70% of the annual rainfall, followed by Argentina, Amazon, Central North America, and India with MCS rainfall fractions around 40-60%. Interestingly, in offshore regions of the east coast of North America and East Asia where enhanced MCS occurrence is observed, MCSs only account for 40% or less of the total rainfall, suggesting other types of precipitation such as those related to extratropical cyclones are more dominant in these regions.

The spatial distribution of MCS rainfall contribution found in this study is qualitatively consistent with previous studies that use different methodologies or observing platforms. Roca et al. (2014) used IR-only tracking to identify MCS during one season (June-September) and showed that MCSs account for 40-60% of tropical rainfall, with a higher percentage over Africa, Bay of Bengal and subtropical Western Pacific. Using low-orbit Microwave Imager overpass precipitation retrieval onboard the TRMM satellite, Nesbitt et al. (2006) defined an MCS simply as a PF with major axis length exceeding 100 km. They also found MCSs dominate precipitation in the tropics with a similar geographic distribution to **Figure 10 c**, although their magnitudes are generally higher (tropics-wide MCS contribution is 60%-70%). This discrepancy could be caused by the lack of temporal continuity of low-orbit satellite observations, or the simplicity of the MCS definition used by Nesbitt et al. (2006). Short-lived convection could grow to reach mesoscale dimension but quickly decay, thus failing the 4-hour duration criterion and not

This article is protected by copyright. All rights reserved.

Accepted Article

included as MCS in this study, as demonstrated by Wang et al. (2019). Results from Nesbitt et al. (2006) possibly overestimated the MCS contribution to the total precipitation, as estimates from YH10 using similar T_b and precipitation data with a more comprehensive method to identify mature MCSs also found a 56% tropical MCS rainfall contribution, more consistent with the current study.

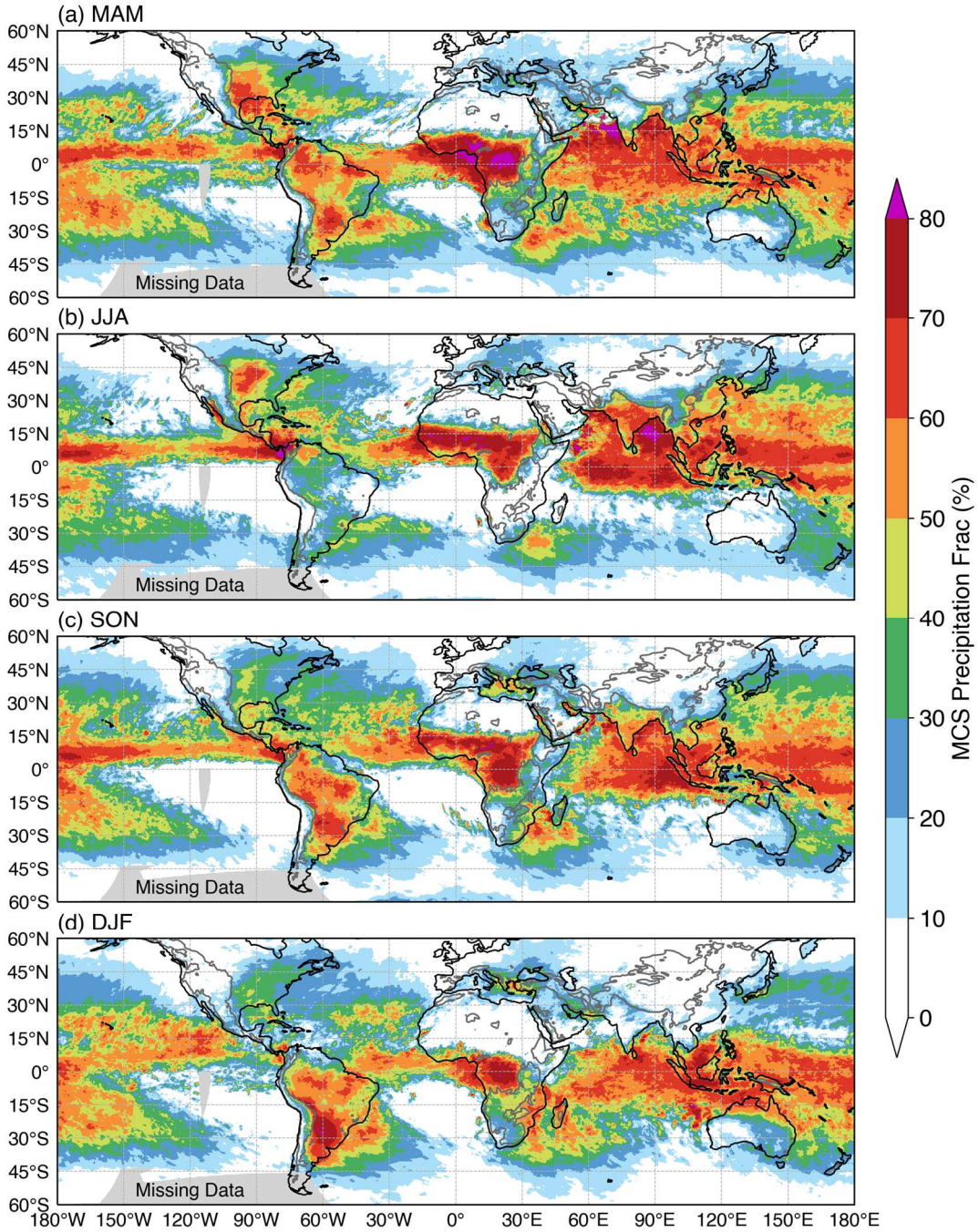

Figure 11. Percentage of MCS precipitation to total precipitation in (a) March-May, (b) June-August, (c) September-November, and (d) December-February.

This article is protected by copyright. All rights reserved.

MCS contribution to regional rainfall displays a strong seasonality over many regions of the globe, except for the Indo-Pacific warm pool and the ITCZ, where MCS consistently accounts for 50-60% of total rainfall throughout the year (**Figure 11)**. Regions with higher MCS seasonal rainfall fractions generally have more MCS occurrence (**Figure S5**) although there are some exceptions (e.g. Northwest Atlantic and Northwest Pacific storm track regions). The MCS numbers shown in **Figure 10a** and **Figure S5** include the effect of MCS PF area, which are larger during the cold season (**Figure S6**) associated with stronger midlatitude baroclinic forcing (Feng et al., 2019). Counting the number of MCS using only the geometric center of MCS PF, a method commonly used in previous studies, results in similar patterns in the tropics, but the midlatitude MCS occurrences during cold seasons are reduced (**Figure S7**), reflecting the impacts of their larger size. During the transition seasons, MCS contributions to total rainfall are higher over the U.S. Great Plains and Eastern China in spring and over the South Asian Monsoon region in both spring and fall. During boreal summer (JJA), MCSs dominate the rainfall over the Central U.S., offshore regions east of North America, South Asian Monsoon region particularly over the Bay of Bengal, East Asian Monsoon region, and the Sahel and Central Africa. During boreal winter (DJF), MCSs account for up to 80% of rainfall in northern Argentina and over 50% offshore to the east of South America and South Africa, the Australian Monsoon region, and subtropical Central Pacific. MCSs account for the smallest total rainfall during the winter season in the respective hemispheres, suggesting non-deep convective synoptic systems are more important in winter when the jet stream moves equatorward and convective instability needed to support MCSs decreases without surface heating and ample moisture. In Europe, while MCSs are less common, they tend to occur more often over the continent in summer and over the Mediterranean Sea during fall and winter, consistent with a previous study that finds a peak in late August to September (Morel & Senesi, 2002). The strong seasonal contrast of MCS occurrences found in this study is quite consistent with previous works that use similar T_b and precipitation data to identify mature MCSs (YH10), and those that use spaceborne radar observations to depict organized convection with deep and/or wide convective features (Wang et al., 2019) and broad stratiform rain regions (Houze et al., 2015).

5.2 MCS lifetime, motion, and rainfall

The more unique aspects of the global MCS tracking database developed in this study are the Lagrangian perspective of the MCSs, the high spatiotemporal resolution, and the collocation of the IR T_b and precipitation data. MCS lifetime and translation speed and direction are two important Lagrangian aspects supported by the analysis of our database. **Figure 12** shows the spatial distribution of average MCS lifetime for JJA and DJF, and the zonal mean MCS lifetime for oceanic and land MCSs. MCS lifetime here is defined by the duration when a significant PF (major axis length > 20 km) is detected within a tracked MCS. This lifetime definition represents the active convection (or precipitation) period of the storm, which is shorter than the lifetime calculated using IR T_b, as the upper-level anvil cloud would persist continuously for some time after convection/precipitation has ended. Results show significant contrast between land and oceanic MCS lifetime in addition to regional and seasonal variability. Long-lived MCSs (lifetime > 36 hours) are primarily found over tropical and subtropical oceans. During JJA, the tropical Eastern Pacific and Eastern Atlantic, the Bay of Bengal and the South China Sea show the longest-lived MCSs (**Figure 12 a)**. These regions feature enhanced synoptic transient disturbances (periods of several days) associated with tropical easterly waves in the summer

This article is protected by copyright. All rights reserved.

Accepted Article

(Lau & Lau, 1990) that potentially create coherence and propagating environments that support long-lived MCSs (Mapes et al., 2006). It is also possible that over ocean multiple convective complexes growing and decaying in close proximity could prolong the MCS lifetime, where such mechanism may be less likely to occur over land. The shortest-lived summer MCSs are found over the interior of the Northern Hemisphere continents such as Canada, Europe, and Siberia. A recent study using GPM DPR data finds extreme deep and wide convective features sometimes occur in these high-latitude continental regions during summer (Houze et al., 2019), suggesting that these extreme convective storms are associated with relatively short-lived MCSs.

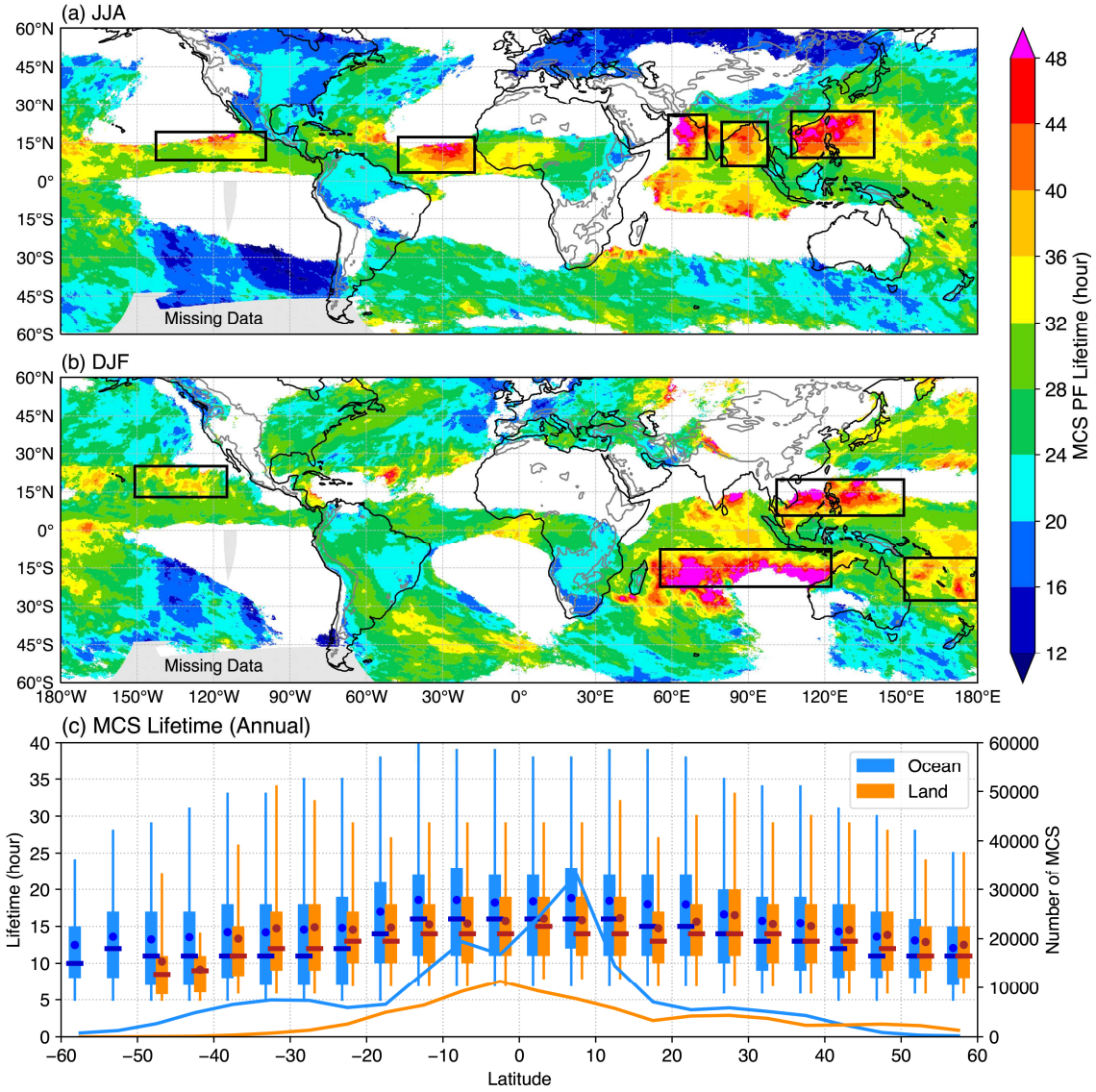

Figure 12. Spatial distribution of mean MCS lifetime during (a) JJA and (b) DJF, (c) box-whisker plot of the zonal MCS lifetime distribution for oceanic and land MCSs. Areas with average number of MCS < 1 are excluded in (a-b). To calculate the spatial distribution, each MCS PF (rain rate > 2 mm h^{-1}) swath during its entire lifetime is assigned a single lifetime value (in hours) on the native 0.1° pixel, and then averaged over time in a season. Regions with long-lived MCS are marked in black boxes, see discussions in the text. In (c), boxes are the interquartile range, horizontal bars are median values, circles are mean values, and whiskers denote 5th and 95th percentile values. The two thick lines in (c) are the number of MCS per latitude bin.

This article is protected by copyright. All rights reserved.

During DJF, long-lived MCSs are more commonly observed near subtropical Eastern Pacific, the tropical Indian Ocean, the Pacific warm pool north of the Maritime Continent and the Southern Pacific Convergence Zone (SPCZ, **Figure 12 b**). Large-scale precipitation systems (duration > 7 days), sometimes associated with the Madden Julian Oscillation (MJO; Madden & Julian, 1972; Zhang, 2005), are frequently observed over the Pacific warm pool during DJF (Kerns & Chen, 2020). The regions with particularly long-lived MCSs are near the fringe of these large-scale precipitation systems or MJOs, suggesting interactions between intraseasonal variability and extra-tropical disturbances may favor long-lived MCS during DJF, which warrants future study. Globally, tropical oceanic MCSs typically last 3-4 hours longer than those over land, but the extreme MCS lifetimes over ocean can be more than 10 hours longer than their land counterparts, particularly around the subtropics (**Figure 12 c**). The land-ocean MCS lifetime contrast gradually diminishes in the mid- and high-latitude where the number of MCSs decreases significantly.

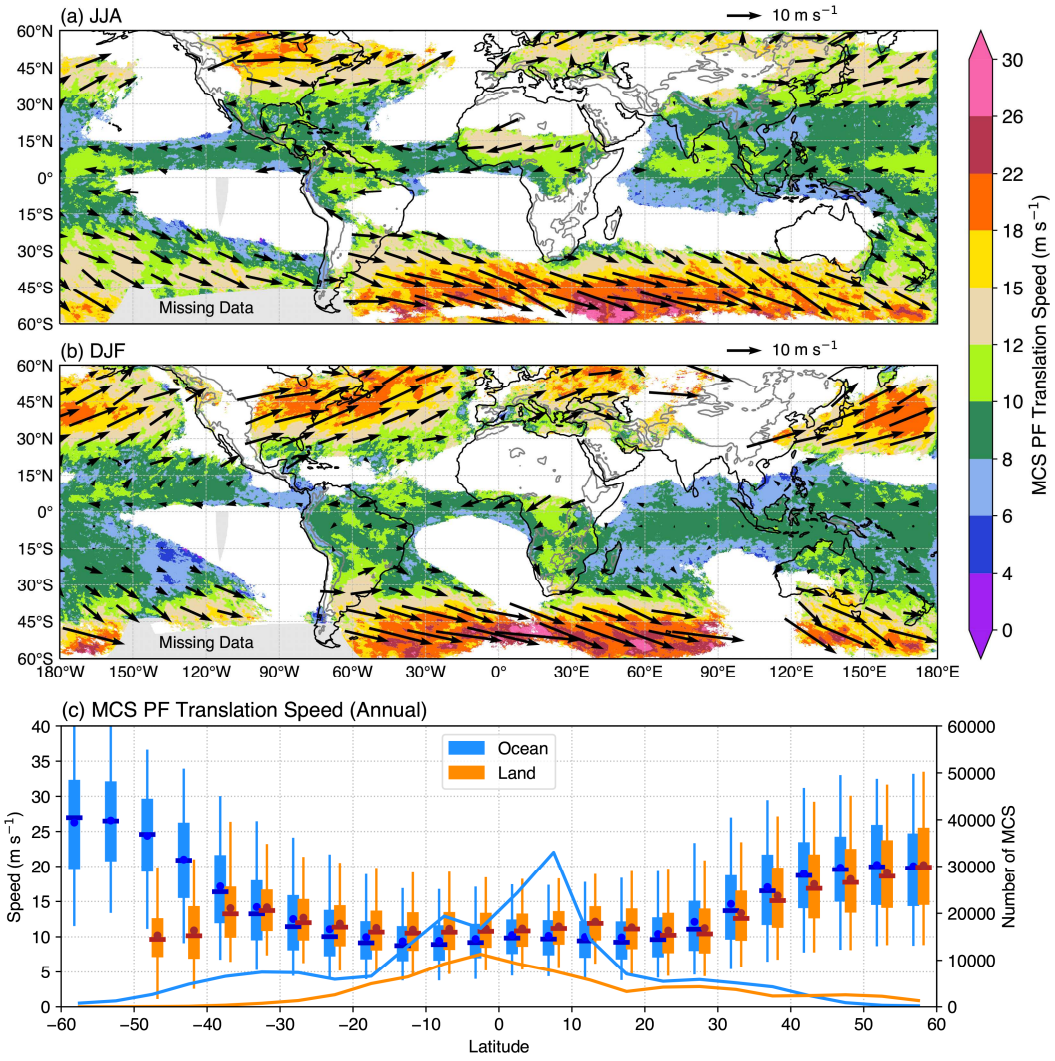

Figure 13. Same as **Figure 12** except for MCS translation speeds and directions. The shadings denote mean translation speed, the vectors show the translation direction and magnitude, which are estimated by

This article is protected by copyright. All rights reserved.

using a 2D cross-correlation map between two consecutive hours of the MCS precipitation features (Feng et al. 2018).

Global distributions of MCS translation speed and direction during JJA and DJF are shown in **Figure 13.** The motion of MCSs is estimated by a 2D cross-correlation map between two consecutive hours of the MCS PFs (Feng et al., 2018) rather than the centroid location difference used in previous methods. This method is less prone to the large fluctuations caused by morphological changes of the MCS cloud or precipitation field that impact the centroid location calculations. There is a strong latitudinal dependence of MCS speed and direction: tropical and subtropical MCSs generally move westward with moderate speeds of 6-12 m s^{-1}, while mid- and high-latitude MCSs move eastward with significantly faster speeds of 12-26 m s^{-1}. The MCS mean translation speeds are generally higher in regions with stronger upper-level zonal wind (e.g., North Atlantic and North Pacific storm tracks during DJF, and Southern Ocean storm tracks during both seasons), suggesting MCSs that occur in traveling disturbances in the stronger westerly jets tend to move faster. However, advection by mid-level wind is only one factor affecting MCS movement. The mid-level wind also affects MCS motion through MCS-induced mesoscale circulations. Other factors such as gravity waves and availability of environmental moisture also affect MCS motion. Using ground-based radar-observed PFs to estimate MCS movement speeds over the U.S., Feng et al. (2019) found similar latitudinal dependence and attributed the probable cause to mesoscale downward transport of stronger background zonal wind velocity at higher latitudes. Compared to the MCS translation speed estimated using NEXRAD radar observations in the U.S. (see Figure 13 and Figure S6 in Feng et al., 2019), the IMERG-based translation speeds are slightly larger during the cold season, suggesting that uncertainties in IMERG precipitation retrievals could potentially affect the translation speed estimates. Interestingly, tropical MCSs over land generally move slightly faster than those over ocean (**Figure 13 c**), particularly over Africa during JJA, suggesting stronger cold pools driven by more rain evaporation over land may help with faster storm movement under relatively weak background wind. This land-ocean contrast in MCS translation speed diminishes in the subtropics and reverses in the mid- to high-latitudes. Cold season MCSs primarily associated with the strongest baroclinic forcing (Feng et al., 2019) show the fastest movement in both respective hemispheres (**Figure 13 a,b**).

The MCS convective intensity and precipitation characteristics between land and ocean across the globe are compared in **Figure 14**. We use the minimum IR T_b (proportional to the deepest cloud-top height) during the entire duration of each MCS as a simple proxy for convective intensity, and similarly use the maximum rain rate during the MCS lifetime to represent the heaviest rainfall intensity. In general, land MCSs have stronger convective intensity than oceanic MCSs (**Figure 14 a**), especially over the subtropical zone (20°-33° in both hemispheres) where land MCSs grow significantly deeper than oceanic MCSs. In contrast, oceanic MCSs produce much more intense precipitation than land MCSs (e.g., median rain rate differs by 10-15 mm h^{-1}, and 95th percentile rain rate differs up to 35 mm h^{-1}), with the largest difference occurring again near the subtropics (**Figure 14 b**). MCSs with the largest maximum rain rates are typically found near the periphery of subtropical highs over the ocean (**Figure S6**) where MCSs are relatively less common (**Figure S5**). These differences in MCS convective intensity and precipitation intensity are likely affected by the fundamental difference in atmospheric environments over land and ocean. For example, higher convective potential

This article is protected by copyright. All rights reserved.

available energy (CAPE) over certain continental regions where deep mixed layer are formed and/or subsidence is produced in the lee of mountain ranges with steep lapse rate and capping inversions can support more intense convection for land MCSs. Intense and highly organized convection such as supercells can produce extreme rainfall in addition to other hazardous weather such as hail and tornadoes (Smith et al., 2001; Nielsen & Schumacher, 2018). It is not immediately clear why oceanic MCSs have significantly higher maximum rainfall intensity compared to their land counterparts. While uncertainties in IMERG precipitation retrieval in intense precipitating MCSs could affect these results (more discussions in Section 5.3), similar land/ocean contrast in maximum MCS rainfall rates is found using the GPM DPR radar-derived surface precipitation data (Figure 4 in Liu et al., 2021). It is possible, however, that both retrievals overestimate ocean rain rates or underestimate land rain rates. More work is needed to systematically compare environmental differences between land and oceanic MCSs to better understand various factors that modulate these MCS characteristics.

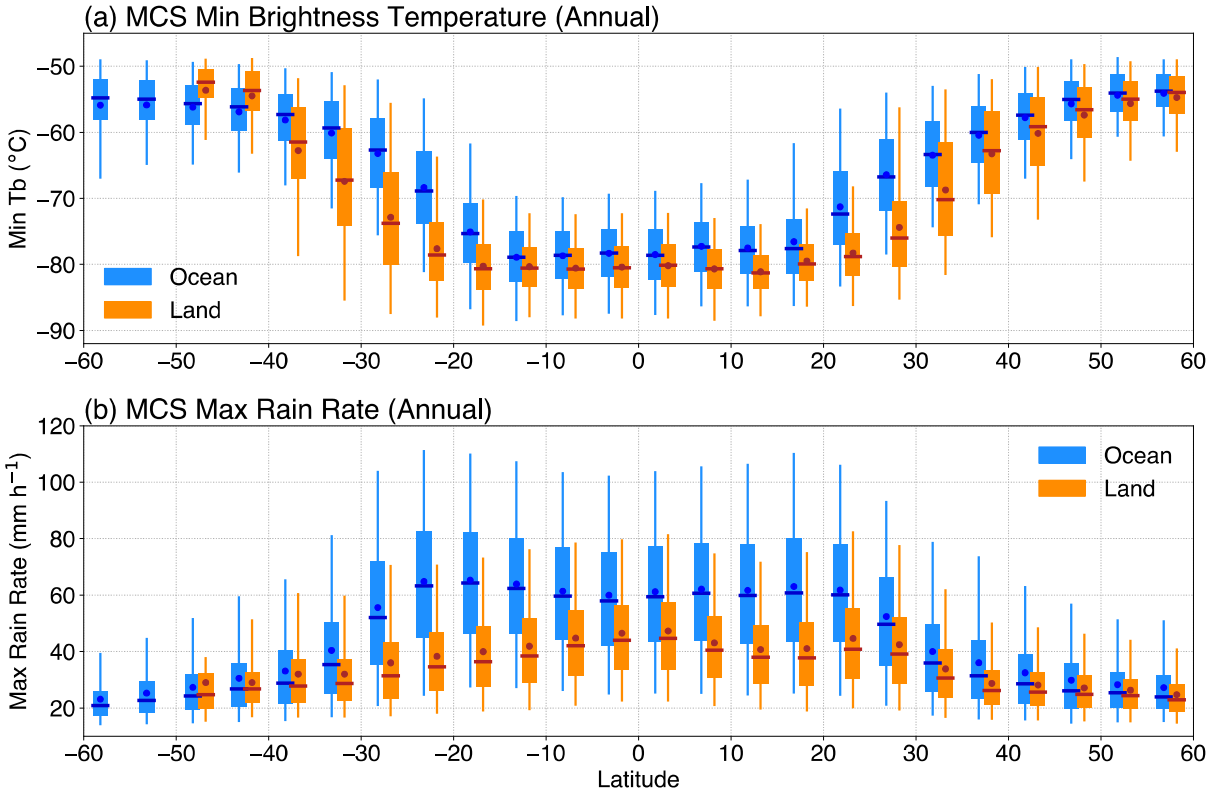

Figure 14. Box-whisker plot of the zonal distribution of (a) minimum IR T_b for each MCS, and (b) maximum rain rate for each MCS. Boxes are the interquartile range, horizontal bars are median values, circles are mean values, and whiskers denote 5th and 95th percentile values.

5.3 Uncertainty of the results

Since various PF criteria are used in this study to identify MCS (Section 3.1), here we briefly examine the sensitivity of the results to the PF parametric thresholds. We lower all four PF parametric thresholds shown in **Figure 3** to examine their impact on MCS frequency and rainfall contribution over different geographic regions. Results show that while the number of MCSs shows a small increase as expected, the impact on MCS precipitation amount and fraction

This article is protected by copyright. All rights reserved.

to total precipitation is less than 10% over most regions (not shown). In Europe, the lower PF criteria increase the annual MCS precipitation fraction by more than 10%, suggesting MCS PF characteristics in Europe are generally weaker, hence lowering the PF parametric thresholds allows more MCSs to be included in that region. This sensitivity test suggests that while using universal criteria to define MCS globally facilitates cross-comparisons among different geographic regions, such an approach may miss some storms in specific regions. In our MCS tracking database, all MCS candidates that satisfy the CCS area and duration are archived, along with their corresponding PF characteristics used to further identify MCS. Therefore, the database allows adjustments of MCS criteria for MCS identification in specific regions without re-running FLEXTRKR, providing more flexibility for future research.

In addition to our MCS tracking methodology, missing geostationary IR T_b data and uncertainties in the IMERG precipitation dataset, including rainfall area and intensity, could also affect the MCS results. Throughout the 20-year period (2000-2019), several generations of geostationary satellite fleets have been used to produce the global MergIR T_b dataset (for a complete list of satellites see https://docserver.gesdisc.eosdis.nasa.gov/public/project/GPM/CPC-4kmIR-Sats.pdf). During the early 2000s, certain regions have larger fractions of missing T_b data (**Figure S9**), such as the West Pacific (130°E - 180°E) and the Southeast Pacific (140°W - 80°W, 60°S - 5°S). We have examined the missing IR T_b data and their impacts on the MCS tracking results on a monthly timescale and found that the impact in the West Pacific region during 2003-2005 is significant. Frequent missing IR T_b data at 4 hours of the day (03, 09, 15, 21 UTC) in that region during those 3 years results in a noticeable reduction of long-lived MCSs and a significant increase of short-lived (5-hour lifetime) ones. Therefore, data between 2003-2005 are excluded in the MCS climatology presented in Section 5. As for the missing data in the Southeast Pacific west of South America (from the Geostationary Operational Environmental Satellite, GOES), while there is a modest amount of missing data (on average 20-30%), the impact on MCS should be relatively small as that region is expected to have few MCSs due to the climatologically low sea surface temperature. In addition, the lack of intercalibration of the MergIR T_b dataset among the multiagency geostationary satellite fleet suggests this database may not be suitable for studying long term trends.

Although MCS statistics obtained from IMERG data have been extensively evaluated over the U.S. and China against ground-based radar datasets, both regions are over midlatitude continents. More evaluations over oceanic regions are needed, as the microwave rainfall estimates used in IMERG were produced using different algorithms for land and ocean. The IMERG data also have known issues such as lack of consistency in consecutive frames, particularly in the near-realtime version of the product (e.g., https://svs.gsfc.nasa.gov/vis/a000000/a004200/a004285/imergert_1080p_30.mp4). Such inconsistency is likely related to the limited availability of microwave-based retrievals at sub-hourly time scale and the “morphing” interpolation technique employed in the IMERG algorithm. Although the final version of the product used in this study with the complete microwave constellations and rain gauge bias correction has improved temporal consistency, fluctuations of hourly rainfall values may affect the accuracy of MCS identification since temporal evolution of PF characteristics is used in our algorithm. However, the PF parameters we use to define MCS are a combination of statistical moments (PF area, mean rain rate, rain rate skewness, heavy rain volume ratio) that are less sensitive to fluctuations of the native pixel-level rainfall values. In addition, our algorithm examines individual continuous sub-periods of each

This article is protected by copyright. All rights reserved.

Accepted Article

tracked cloud system when a PF reaches mesoscale dimension (PF major axis length > 100 km). If the PF parameters during that sub-period exceed their respective thresholds determined by the sub-period duration (at least 5 hours), the entire tracked cloud system is identified as an MCS. As long as the IMERG-derived PF parameters do not consistently drop below the minimum thresholds more frequently than 5 hours, the fluctuations should not impact MCS identification.

The IMERG microwave rainfall retrievals are calibrated against the combined radar-radiometer algorithm, which could transfer the limitations of the radar retrieval scheme (Huffman, Bolvin, Braithwaite, et al., 2019; Huffman, Bolvin, Nelkin, et al., 2019). Previous studies have shown that the TRMM radar retrieved surface precipitation in intense convective cores over land are underestimated due to biases in attenuation correction associated with hail/graupel (Rasmussen et al., 2013; Gingrey et al., 2018). Since similar radar-radiometer rainfall retrieval scheme is used in GPM rainfall products, such biases could potentially affect microwave retrievals that are used in the IMERG precipitation data. More comparisons on intense convective precipitation retrievals both over ocean and land from IMERG against ground-based radar estimates, such as radars located on coastal regions and remote islands in the tropics and subtropics could further shed light on intense MCS rainfall contrast between land and ocean.

Newly available high-resolution satellite precipitation data product such as GPM IMERG should be treated as experimental global datasets. Uncertainties in these retrievals may impact the accuracy of the global MCS climatology results presented in this study. Nevertheless, the physically sound MCS features, including their geographical and seasonal variations, land vs. ocean contrasts and consistency with previous studies using independent satellite observations suggest that the IMERG dataset is capable of supporting our effort in developing a long-term high-resolution global MCS tracking database and providing a global survey of MCS characteristics. When improved versions of IMERG products become available in future, the global MCS dataset developed in this study will be updated accordingly.

6 Summary and Conclusions

In this study, we develop a new methodology to construct a global (60°S – 60°N) long-term (2000-2019) high-resolution (~10 km, 1 hourly) MCS database by jointly using geostationary satellite infrared brightness temperature (IR T_b) and the GPM IMERG precipitation datasets. The method characterizes MCSs by both combining T_b and precipitation feature (PF) fields and tracking the features over time. Previous techniques have used either tracking only T_b features in time (e.g., Roca et al., 2014; Huang et al., 2018) or combining T_b and precipitation without tracking (YH10).

MCSs in this study must satisfy both large cold cloud shield and mesoscale PF requirements for longer than 4 hours (see details in Section 3.1). The PF characteristics are calibrated with a long-term MCS dataset based on the NEXRAD radar network in the U.S. (Feng, 2019). MCS statistics obtained using the satellite-based IMERG data are validated against two midlatitude continental ground-based radar networks (NEXRAD in the U.S. and the operational radar network in northern China). The validation results show that our methodology detects MCSs with a wide range of sizes and strengths comparable to those observed by radar networks. In addition, the MCS climatology obtained in the near-equatorial latitudes is consistent

This article is protected by copyright. All rights reserved.

Accepted Article

with that obtained by YH10 using T_b and precipitation but without tracking. These evaluations provide confidence in applying our algorithm globally.

Our analyses show that previous IR-only tracking method significantly overestimates MCS occurrences in the midlatitudes in all seasons except summer compared to the new IR+PF method (**Figure 8**). The false identification by the IR-only method is related to many large and long-lived cloud systems containing very small PFs with low rainfall intensity and stratiform-like precipitation, inconsistent with MCS precipitation characteristics. Such comparisons highlight the advancement of our new method that carefully considers key PF characteristics in addition to the cloud-top IR signature to identify MCS. We apply this new algorithm on the global satellite T_b and IMERG data obtained during 2001-2019 to examine the climatology of global MCS characteristics.

Our results are consistent with YH10 in showing that in the deep tropics the largest number of MCSs are over the Indo-Pacific warm pool, Central Africa, the Amazon and Eastern Tropical Pacific. In midlatitudes, the most MCSs occur in the central U.S., Argentina and offshore of the east coast of North America, South America, East Asia and South Africa. MCS precipitation contributions exceeds 50% of the annual total precipitation across a majority of the tropical belt, such as the Indo-Pacific warm pool, Bay of Bengal, tropical Eastern Atlantic and tropical Eastern Pacific. Over continents, MCS rainfall fraction over the West African Monsoon region exceeds 70%, followed by Argentina, the Amazon, Central North America and India with fractions around 40-60%. A strong seasonality of MCS occurrence and rainfall contribution is found over many regions of the globe (**Figure 11**).

In addition to regional and seasonal variability, a significant contrast between land and oceanic MCS lifetime is found. Long-lived MCSs (lifetime > 36 hours) are primarily found over tropical and subtropical oceans, particularly over the tropical Eastern Pacific and Eastern Atlantic, the Bay of Bengal and South China Sea during JJA, and subtropical Eastern Pacific, tropical Indian Ocean, and the Pacific warm pool and SPCZ during DJF (**Figure 12**). We find a strong latitudinal dependence of the speed and direction of MCS movement. Tropical and subtropical MCSs generally move westward with moderate speeds of 6-12 m s^{-1}, while mid- and high-latitude MCSs predominately move eastward with significantly greater speeds of 12-26 m s^{-1} (**Figure 13**). Convective intensity and precipitation characteristics also show notable contrasts between land and oceanic MCSs. Land MCSs have stronger convective intensity than oceanic MCSs for most regions of the globe, particularly over the subtropics (**Figure 14**). In contrast, oceanic MCSs produce more heavy precipitation than land MCSs, suggesting the fundamental differences in favorable storm environments such as atmospheric instability and moisture availability that could affect these MCS characteristics, although further studies are needed to better understand the relative importance of various environmental factors.

With the global MCS tracking database developed in this study we have produced a fully global climatology of MCSs. Past studies have generally been limited to certain regions or have been limited by the inadequacy of tracking only T_b features. This global climatology based on T_b, precipitation, and tracking, has high spatiotemporal resolution, a large sample size (~30,000 MCSs per year), and long-term availability (2000-2019). These properties allow for a broad range of regional and global research applications. For example, the diverse environmental factors that impact MCS formation, evolution, and strength over different geographic regions may now be pursued in follow-on studies. The role of MCSs in global and regional hydrologic cycles, and their interactions with large-scale circulations such as monsoon systems and modes

This article is protected by copyright. All rights reserved.

Accepted Article

of variability such as the MJO are already under investigation. The global MCS dataset is also suitable for evaluating the performance of both global and regional climate models, particularly in regions without extensive ground-based observation networks. Combining this database with TRMM and GPM radar PF and latent heating products, we are developing a new dataset to characterize the spatiotemporal variability of global MCS latent heating (Liu et al., 2021) to support observational and modeling studies of MCSs and their characteristics.

Accepted Article

This article is protected by copyright. All rights reserved.

Accepted Article

Acknowledgments, Samples, and Data

This study is supported by the U.S. Department of Energy Office of Science Biological and Environmental Research (BER) as part of the Regional and Global Climate Modeling program through the Water Cycle and Climate Extremes Modeling (WACCEM) scientific focus area. The authors thank Dr. Adam Varble for his insightful discussions and comments to improve the manuscript. Development of the MCS tracking method and data analyses described in this study were performed using computational resources provided by the National Energy Research Scientific Computing Center (NERSC), a DOE Office of Science User Facility supported by the Office of Science of the U.S. Department of Energy under contract DE-AC02-05CH11231. PNNL is operated for DOE by Battelle Memorial Institute under contract DE-AC05-76RL01830. The Global Merged IR dataset is obtained at NASA Goddard Earth Sciences Data and Information Services Center (https://doi.org/10.5067/P4HZB9N27EKU). The GPM IMERG precipitation data V06 (Huffman, Stocker, et al., 2019) are obtained from the NASA Goddard Earth Sciences Data and Information Services Center (https://doi.org/10.5067/GPM/IMERG/3B-HH/06). The NEXRAD MCS database over the U.S. is obtained from the Atmospheric Radiation Measurement program (https://doi.org/10.5439/1571643). The China radar dataset is obtained from the National Meteorological Information Center, China Meteorological Administration (http://data.cma.cn/en/?r=data/index&cid=227aa07a9079550a). The IBTrACS tropical cyclone database v4 is obtained from the NOAA National Climatic Data Center (https://doi.org/10.25921/82ty-9e16). We thank Dr. Allison Collow for providing the global high-resolution Atmospheric River database as part of the Atmospheric River Tracking Method Intercomparison Project (ARTMIP). ARTMIP is a grassroots community effort and includes a collection of international researchers from universities, laboratories, and agencies. Cochairs and committee members include Jonathan Rutz, Christine Shields, L. Ruby Leung, F. Martin Ralph, Michael Wehner, Ashley Payne, and Travis O'Brien. Details on catalogues developers can be found on the ARTMIP website. ARTMIP has received support from the U.S. Department of Energy Office of Science Biological and Environmental Research (BER) as part of the Regional and Global Climate Modeling program, and the Center for Western Weather and Water Extremes (CW3E) at Scripps Institute for Oceanography at the University of California, San Diego. The global MCS dataset is archived at the NERSC High Performance Storage System (HPSS): /home/f/feng045/GPM/. The final processed data used to generate the figures in the study can be accessed at https://doi.org/10.5281/zenodo.4244985.

This article is protected by copyright. All rights reserved.

References

Ashley, W. S., & Mote, T. L. (2005). Derecho Hazards in the United States. *Bulletin of the American Meteorological Society, 86*(11), 1577-1592. http://dx.doi.org/10.1175/BAMS-86-11-1577

Bowman, K. P., & Homeyer, C. R. (2017). *GridRad - Three-Dimensional Gridded NEXRAD WSR-88D Radar Data*. Retrieved from: https://doi.org/10.5065/D6NK3CR7

Cannon, F., Cordeira, J. M., Hecht, C. W., Norris, J. R., Michaelis, A., Demirdjian, R., & Ralph, F. M. (2020). GPM Satellite Radar Observations of Precipitation Mechanisms in Atmospheric Rivers. *Monthly Weather Review, 148*(4), 1449-1463. https://journals.ametsoc.org/doi/abs/10.1175/MWR-D-19-0278.1

Chen, D., Guo, J., Yao, D., Feng, Z., & Lin, Y. (2020). Elucidating the Life Cycle of Warm-Season Mesoscale Convective Systems in Eastern China from the Himawari-8 Geostationary Satellite. *Remote Sensing, 12*(14). https://doi.org/10.3390/rs12142307

Chen, D. D., Guo, J. P., Yao, D., Lin, Y. L., Zhao, C. F., Min, M., et al. (2019). Mesoscale Convective Systems in the Asian Monsoon Region From Advanced Himawari Imager: Algorithms and Preliminary Results. *Journal of Geophysical Research-Atmospheres, 124*(4), 2210-2234. https://doi.org/10.1029/2018JD029707

Creamean, J. M., Suski, K. J., Rosenfeld, D., Cazorla, A., DeMott, P. J., Sullivan, R. C., et al. (2013). Dust and Biological Aerosols from the Sahara and Asia Influence Precipitation in the Western U.S. *Science, 339*(6127), 1572-1578. https://science.sciencemag.org/content/sci/339/6127/1572.full.pdf

Cui, W., Dong, X., Xi, B., Feng, Z., & Fan, J. (2020). Can the GPM IMERG Final Product Accurately Represent MCSs' Precipitation Characteristics over the Central and Eastern United States? *Journal of Hydrometeorology, 21*(1), 39-57. https://journals.ametsoc.org/doi/abs/10.1175/JHM-D-19-0123.1

Doswell, C. A., Brooks, H. E., & Maddox, R. A. (1996). Flash Flood Forecasting: An Ingredients-Based Methodology. *Weather and Forecasting, 11*(4), 560-581. https://journals.ametsoc.org/doi/abs/10.1175/1520-0434%281996%29011%3C0560%3AFFFAIB%3E2.0.CO%3B2

Feng, Z. (2019). *Mesoscale convective system (MCS) database over United States*. Retrieved from: https://doi.org/10.5439/1571643

Feng, Z., Houze, R. A., Leung, L. R., Song, F., Hardin, J. C., Wang, J., et al. (2019). Spatiotemporal Characteristics and Large-scale Environments of Mesoscale Convective Systems East of the Rocky Mountains. *Journal of Climate, 32*(21), 7303-7328. https://doi.org/10.1175/JCLI-D-19-0137.1

Feng, Z., Leung, L. R., Hagos, S., Houze, R. A., Burleyson, C. D., & Balaguru, K. (2016). More frequent intense and long-lived storms dominate the springtime trend in central US rainfall. *Nat Commun, 7*, 13429. https://www.ncbi.nlm.nih.gov/pubmed/27834368

Feng, Z., Leung, L. R., Houze, R. A., Hagos, S., Hardin, J., Yang, Q., et al. (2018). Structure and Evolution of Mesoscale Convective Systems: Sensitivity to Cloud Microphysics in Convection-Permitting Simulations Over the United States. *Journal of Advances in Modeling Earth Systems, 10*(7), 1470-1494. https://doi.org/10.1029/2018MS001305

Feng, Z., Song, F., Sakaguchi, K., & Leung, L. R. (2020). Evaluation of Mesoscale Convective Systems in Climate Simulations: Methodological Development and Results from MPAS-CAM over the U.S. *Journal of Climate*, 1-62. https://doi.org/10.1175/JCLI-D-20-0136.1

Fiolleau, T., & Roca, R. (2013). An Algorithm for the Detection and Tracking of Tropical Mesoscale Convective Systems Using Infrared Images From Geostationary Satellite. *IEEE Transactions on Geoscience and Remote Sensing, 51*(7), 4302-4315.

Fiolleau, T., Roca, R., Cloché, S., Bouniol, D., & Raberanto, P. (2020). Homogenization of Geostationary Infrared Imager Channels for Cold Cloud Studies Using Megha-Tropiques/ScaRaB. *IEEE Transactions on Geoscience and Remote Sensing, 58*(9), 6609-6622.

Fritsch, J. M., Kane, R. J., & Chelius, C. R. (1986). The Contribution of Mesoscale Convective Weather Systems to the Warm-Season Precipitation in the United States. *Journal of Climate and Applied Meteorology, 25*(10), 1333-1345. http://dx.doi.org/10.1175/1520-0450(1986)025<1333:TCOMCW>2.0.CO;2

Futyan, J. M., & Del Genio, A. D. (2007). Deep Convective System Evolution over Africa and the Tropical Atlantic. *Journal of Climate, 20*(20), 5041-5060. http://dx.doi.org/10.1175/JCLI4297.1

Gingrey, A., Varble, A., & Zipser, E. (2018). Relationships between Extreme Rain Rates and Convective Intensities from the Perspectives of TRMM and WSR-88D Radars. *Journal of Applied Meteorology and Climatology, 57*(6), 1353-1369. https://doi.org/10.1175/JAMC-D-17-0240.1

This article is protected by copyright. All rights reserved.

Haberlie, A. M., & Ashley, W. S. (2019). A Radar-Based Climatology of Mesoscale Convective Systems in the United States. *Journal of Climate*, *32*(5), 1591-1606. https://journals.ametsoc.org/doi/abs/10.1175/JCLI-D-18-0559.1

Haertel, P. T., & Kiladis, G. N. (2004). Dynamics of 2-Day Equatorial Waves. *Journal of the Atmospheric Sciences*, *61*(22), 2707-2721. https://journals.ametsoc.org/doi/abs/10.1175/JAS3352.1

Houze, R. A. (1997). Stratiform Precipitation in Regions of Convection: A Meteorological Paradox? *Bulletin of the American Meteorological Society*, *78*(10), 2179-2196. http://dx.doi.org/10.1175/1520-0477(1997)078<2179:SPIROC>2.0.CO;2

Houze, R. A. (2004). Mesoscale convective systems. *Reviews of Geophysics*, *42*(4), RG4003. http://dx.doi.org/10.1029/2004RG000150

Houze, R. A. (2014). *Cloud Dynamics* (2nd ed.): Elsevier/Academic Press, Oxford.

Houze, R. A. (2018). 100 Years of Research on Mesoscale Convective Systems. *Meteorological Monographs*, *59*, 17.11-17.54. https://journals.ametsoc.org/doi/abs/10.1175/AMSMONOGRAPHS-D-18-0001.1

Houze, R. A., Jr., Rasmussen, K. L., Zuluaga, M. D., & Brodzik, S. R. (2015). The variable nature of convection in the tropics and subtropics: A legacy of 16 years of the Tropical Rainfall Measuring Mission satellite. *Rev Geophys*, *53*(3), 994-1021. https://www.ncbi.nlm.nih.gov/pubmed/27668295

Houze, R. A., Smull, B. F., & Dodge, P. (1990). Mesoscale Organization of Springtime Rainstorms in Oklahoma. *Monthly Weather Review*, *118*(3), 613-654. http://dx.doi.org/10.1175/1520-0493(1990)118<0613:MOOSRI>2.0.CO;2

Houze, R. A., Wang, J., Fan, J., Brodzik, S., & Feng, Z. (2019). Extreme Convective Storms Over High-Latitude Continental Areas Where Maximum Warming Is Occurring. *Geophysical Research Letters*, *46*(7), 4059-4065. https://agupubs.onlinelibrary.wiley.com/doi/abs/10.1029/2019GL082414

Huang, X., Hu, C., Huang, X., Chu, Y., Tseng, Y.-h., Zhang, G. J., & Lin, Y. (2018). A long-term tropical mesoscale convective systems dataset based on a novel objective automatic tracking algorithm. *Climate Dynamics*. journal article. https://doi.org/10.1007/s00382-018-4071-0

Huffman, G. J., Bolvin, D. T., Braithwaite, D., Hsu, K., Joyce, R., Kidd, C., et al. (2019). *Algorithm Theoretical Basis Document (ATBD) Version 06. NASA Global Precipitation Measurement (GPM) Integrated Multi-satellitE Retrievals for GPM (IMERG) (Algorithm Theoretical Basis Document)*. Retrieved from NASA: https://pmm.nasa.gov/data-access/downloads/gpm

Huffman, G. J., Bolvin, D. T., Nelkin, E. J., & Tan, J. (2019). *Integrated Multi-satellitE Retrievals for GPM (IMERG) technical documentation (technical documentation)*. Retrieved from NASA: https://pmm.nasa.gov/data-access/downloads/gpm

Huffman, G. J., Stocker, E. F., Bolvin, D. T., Nelkin, E. J., & Tan, J. (2019). *GPM IMERG Final Precipitation L3 Half Hourly 0.1 degree x 0.1 degree V06*. Retrieved from: ftp://arthurhou.pps.eosdis.nasa.gov/gpmdata/

Janowiak, J., Joyce, B., & Xie, P. (2017). *NCEP/CPC L3 Half Hourly 4km Global (60S - 60N) Merged IR V1*. Retrieved from: https://doi.org/10.5067/P4HZB9N27EKU

Jirak, I. L., Cotton, W. R., & McAnelly, R. L. (2003). Satellite and Radar Survey of Mesoscale Convective System Development. *Monthly Weather Review*, *131*(10), 2428-2449. http://dx.doi.org/10.1175/1520-0493(2003)131<2428:SARSOM>2.0.CO;2

Kerns, B. W., & Chen, S. S. (2020). A 20-Year Climatology of Madden-Julian Oscillation Convection: Large-Scale Precipitation Tracking From TRMM-GPM Rainfall. *Journal of Geophysical Research: Atmospheres*, *125*(7), e2019JD032142. https://agupubs.onlinelibrary.wiley.com/doi/abs/10.1029/2019JD032142

Klein, C., Belušić, D., & Taylor, C. M. (2018). Wavelet Scale Analysis of Mesoscale Convective Systems for Detecting Deep Convection From Infrared Imagery. *Journal of Geophysical Research: Atmospheres*, *123*(6), 3035-3050. https://agupubs.onlinelibrary.wiley.com/doi/abs/10.1002/2017JD027432

Knapp, K. R., Diamond, H. J., Kossin, J. P., Kruk, M. C., & Schreck, C. J. I. (2018). *International Best Track Archive for Climate Stewardship (IBTrACS) Project, Version 4*. Retrieved from: https://doi.org/10.25921/82ty-9e16

Knapp, K. R., Kruk, M. C., Levinson, D. H., Diamond, H. J., & Neumann, C. J. (2010). The International Best Track Archive for Climate Stewardship (IBTrACS): Unifying Tropical Cyclone Data. *Bulletin of the American Meteorological Society*, *91*(3), 363-376. https://doi.org/10.1175/2009BAMS2755.1

Kummerow, C., Hong, Y., Olson, W. S., Yang, S., Adler, R. F., McCollum, J., et al. (2001). The Evolution of the Goddard Profiling Algorithm (GPROF) for Rainfall Estimation from Passive Microwave Sensors. *Journal of Applied Meteorology*, *40*(11), 1801-1820. http://dx.doi.org/10.1175/1520-0450(2001)040<1801:TEOTGP>2.0.CO;2

This article is protected by copyright. All rights reserved.

Kummerow, C. D., Randel, D. L., Kulie, M., Wang, N.-Y., Ferraro, R., Munchak, S. J., & Petkovic, V. (2015). The Evolution of the Goddard Profiling Algorithm to a Fully Parametric Scheme. *Journal of Atmospheric and Oceanic Technology, 32*(12), 2265-2280. https://journals.ametsoc.org/doi/abs/10.1175/JTECH-D-15-0039.1

Kummerow, C. D., Ringerud, S., Crook, J., Randel, D., & Berg, W. (2011). An Observationally Generated A Priori Database for Microwave Rainfall Retrievals. *Journal of Atmospheric and Oceanic Technology, 28*(2), 113-130. https://journals.ametsoc.org/doi/abs/10.1175/2010JTECHA1468.1

Laing, A. G., & Fritsch, J. M. (1997). The global population of mesoscale convective complexes. *Quarterly Journal of the Royal Meteorological Society, 123*(538), 389-405. <Go to ISI>://WOS:A1997WN08000006

Laing, A. G., & Fritsch, J. M. (2000). The large-scale environments of the global populations of mesoscale convective complexes. *Monthly Weather Review, 128*(8), 2756-2776. <Go to ISI>://WOS:000088849600008

Lau, K.-H., & Lau, N.-C. (1990). Observed Structure and Propagation Characteristics of Tropical Summertime Synoptic Scale Disturbances. *Monthly Weather Review, 118*(9), 1888-1913. https://doi.org/10.1175/1520-0493(1990)118<1888:OSAPCO>2.0.CO;2

Lin, Y. (2011). *GCIP/EOP Surface: Precipitation NCEP/EMC 4KM Gridded Data (GRIB) Stage IV Data. Version 1.0.*

Liu, C., Shige, S., Takayabu, Y. N., & Zipser, E. (2015). Latent Heating Contribution from Precipitation Systems with Different Sizes, Depths, and Intensities in the Tropics. *Journal of Climate, 28*(1), 186-203. https://journals.ametsoc.org/doi/abs/10.1175/JCLI-D-14-00370.1

Liu, C. T., & Zipser, E. (2013). Regional variation of morphology of organized convection in the tropics and subtropics. *Journal of Geophysical Research-Atmospheres, 118*(2), 453-466. https://doi.org/10.1029/2012JD018409

Liu, N., Leung, L. R., & Feng, Z. (2021). Global Mesoscale Convective System Latent Heating Characteristics from GPM Retrievals and an MCS Tracking Dataset. *Journal of Climate, Submitted*.

Machado, L. A. T., Rossow, W. B., Guedes, R. L., & Walker, A. W. (1998). Life cycle variations of mesoscale convective systems over the Americas. *Monthly Weather Review, 126*(6), 1630-1654. <Go to ISI>://WOS:000074834700013

Madden, R. A., & Julian, P. R. (1972). Description of Global-Scale Circulation Cells in the Tropics with a 40–50 Day Period. *Journal of the Atmospheric Sciences, 29*(6), 1109-1123. http://dx.doi.org/10.1175/1520-0469(1972)029<1109:DOGSCC>2.0.CO;2

Maddox, R. A. (1980). Meoscale Convective Complexes. *Bulletin of the American Meteorological Society, 61*(11), 1374-1387. http://dx.doi.org/10.1175/1520-0477(1980)061<1374:MCC>2.0.CO;2

Mapes, B., Tulich, S., Lin, J., & Zuidema, P. (2006). The mesoscale convection life cycle: Building block or prototype for large-scale tropical waves? *Dynamics of Atmospheres and Oceans, 42*(1-4), 3-29. <Go to ISI>://WOS:000242272200002

Moncrieff, M. W. (2010). The Multiscale Organization of Moist Convection and the Intersection of Weather and Climate. In D.-Z. Sun & F. Bryan (Eds.), *Climate Dynamics: Why Does Climate Vary?* (Vol. 189, pp. 3-26). Geophys. Monogr.: American Geophysical Union.

Moore, B. J., Neiman, P. J., Ralph, F. M., & Barthold, F. E. (2012). Physical Processes Associated with Heavy Flooding Rainfall in Nashville, Tennessee, and Vicinity during 1–2 May 2010: The Role of an Atmospheric River and Mesoscale Convective Systems*. *Monthly Weather Review, 140*(2), 358-378. https://doi.org/10.1175/MWR-D-11-00126.1

Morel, C., & Senesi, S. (2002). A climatology of mesoscale convective systems over Europe using satellite infrared imagery. II: Characteristics of European mesoscale convective systems. *Quarterly Journal of the Royal Meteorological Society, 128*(584), 1973-1995. <Go to ISI>://WOS:000177646300010

Nesbitt, S. W., Cifelli, R., & Rutledge, S. A. (2006). Storm morphology and rainfall characteristics of TRMM precipitation features. *Monthly Weather Review, 134*(10), 2702-2721. <Go to ISI>://WOS:000241361900004

Nielsen, E. R., & Schumacher, R. S. (2018). Dynamical Insights into Extreme Short-Term Precipitation Associated with Supercells and Mesovortices. *Journal of the Atmospheric Sciences, 75*(9), 2983-3009. https://journals.ametsoc.org/view/journals/atsc/75/9/jas-d-17-0385.1.xml

Rasmussen, K. L., Choi, S. L., Zuluaga, M. D., & Houze Jr., R. A. (2013). TRMM precipitation bias in extreme storms in South America. *Geophysical Research Letters, 40*(13), 3457-3461. https://agupubs.onlinelibrary.wiley.com/doi/abs/10.1002/grl.50651

This article is protected by copyright. All rights reserved.

Accepted Article

Roca, R., Aublanc, J., Chambon, P., Fiolleau, T., & Viltard, N. (2014). Robust Observational Quantification of the Contribution of Mesoscale Convective Systems to Rainfall in the Tropics. *Journal of Climate*, *27*(13), 4952-4958. http://dx.doi.org/10.1175/JCLI-D-13-00628.1

Roca, R., Fiolleau, T., & Bouniol, D. (2017). A Simple Model of the Life Cycle of Mesoscale Convective Systems Cloud Shield in the Tropics. *Journal of Climate*, *30*(11), 4283-4298. https://journals.ametsoc.org/doi/abs/10.1175/JCLI-D-16-0556.1

Rutz, J. J., Shields, C. A., Lora, J. M., Payne, A. E., Guan, B., Ullrich, P., et al. (2019). The Atmospheric River Tracking Method Intercomparison Project (ARTMIP): Quantifying Uncertainties in Atmospheric River Climatology. *Journal of Geophysical Research: Atmospheres*, *124*(24), 13777-13802. https://agupubs.onlinelibrary.wiley.com/doi/abs/10.1029/2019JD030936

Schumacher, C., & Houze, R. A. (2003). Stratiform rain in the tropics as seen by the TRMM precipitation radar. *Journal of Climate*, *16*(11), 1739-1756. https://doi.org/10.1175/1520-0442(2003)016<1739:SRITTA>2.0.CO;2

Schumacher, C., & Houze, R. A. (2006). Stratiform precipitation production over sub-Saharan Africa and the tropical East Atlantic as observed by TRMM. *Quarterly Journal of the Royal Meteorological Society*, *132*(620), 2235-2255. <Go to ISI>://WOS:000242468800007

Schumacher, C., Houze, R. A., & Kraucunas, I. (2004). The tropical dynamical response to latent heating estimates derived from the TRMM precipitation radar. *Journal of the Atmospheric Sciences*, *61*(12), 1341-1358. https://doi.org/10.1175/1520-0469(2004)061<1341:TTDRTL>2.0.CO;2

Shige, S., Takayabu, Y. N., Tao, W.-K., & Shie, C.-L. (2007). Spectral Retrieval of Latent Heating Profiles from TRMM PR Data. Part II: Algorithm Improvement and Heating Estimates over Tropical Ocean Regions. *Journal of Applied Meteorology and Climatology*, *46*(7), 1098-1124. http://dx.doi.org/10.1175/JAM2510.1

Smith, B. T., Thompson, R. L., Grams, J. S., Broyles, C., & Brooks, H. E. (2012). Convective Modes for Significant Severe Thunderstorms in the Contiguous United States. Part I: Storm Classification and Climatology. *Weather and Forecasting*, *27*(5), 1114-1135. <Go to ISI>://WOS:000310096800003

Smith, J. A., Baeck, M. L., Zhang, Y., & Doswell, C. A. (2001). Extreme Rainfall and Flooding from Supercell Thunderstorms. *Journal of Hydrometeorology*, *2*(5), 469-489. https://journals.ametsoc.org/view/journals/hydr/2/5/1525-7541_2001_002_0469_eraffs_2_0_co_2.xml

Stephens, G. L., Vane, D. G., Boain, R. J., Mace, G. G., Sassen, K., Wang, Z., et al. (2002). THE CLOUDSAT MISSION AND THE A-TRAIN. *Bulletin of the American Meteorological Society*, *83*(12), 1771-1790. http://dx.doi.org/10.1175/BAMS-83-12-1771

Stevenson, S. N., & Schumacher, R. S. (2014). A 10-Year Survey of Extreme Rainfall Events in the Central and Eastern United States Using Gridded Multisensor Precipitation Analyses. *Monthly Weather Review*, *142*(9), 3147-3162. http://dx.doi.org/10.1175/MWR-D-13-00345.1

Tan, J., Huffman, G. J., Bolvin, D. T., & Nelkin, E. J. (2019a). Diurnal Cycle of IMERG V06 Precipitation. *Geophysical Research Letters*, *46*(22), 13584-13592. https://agupubs.onlinelibrary.wiley.com/doi/abs/10.1029/2019GL085395

Tan, J., Huffman, G. J., Bolvin, D. T., & Nelkin, E. J. (2019b). IMERG V06: Changes to the Morphing Algorithm. *Journal of Atmospheric and Oceanic Technology*, *36*(12), 2471-2482. https://journals.ametsoc.org/doi/abs/10.1175/JTECH-D-19-0114.1

Tao, W.-K., Smith, E. A., Adler, R. F., Haddad, Z. S., Hou, A. Y., Iguchi, T., et al. (2006). Retrieval of Latent Heating from TRMM Measurements. *Bulletin of the American Meteorological Society*, *87*(11), 1555-1572. https://journals.ametsoc.org/doi/abs/10.1175/BAMS-87-11-1555

Wang, J. Y., Houze, R. A., Fan, J. W., Brodzik, S. R., Feng, Z., & Hardin, J. C. (2019). The Detection of Mesoscale Convective Systems by the GPM Ku-Band Spaceborne Radar. *Journal of the Meteorological Society of Japan*, *97*(6), 1059-1073. https://doi.org/10.2151/jmsj.2019-058

Yang, Q., Houze, R. A., Leung, L. R., & Feng, Z. (2017). Environments of Long-Lived Mesoscale Convective Systems Over the Central United States in Convection Permitting Climate Simulations. *Journal of Geophysical Research: Atmospheres*, *122*(24), 13,288-213,307. http://dx.doi.org/10.1002/2017JD027033

Yang, X. R., Fei, J. F., Huang, X. G., Cheng, X. P., Carvalho, L. M. V., & He, H. R. (2015). Characteristics of Mesoscale Convective Systems over China and Its Vicinity Using Geostationary Satellite FY2. *Journal of Climate*, *28*(12), 4890-4907. <Go to ISI>://WOS:000356283900016

Yuan, J., & Houze, R. A. (2010). Global Variability of Mesoscale Convective System Anvil Structure from A-Train Satellite Data. *Journal of Climate*, *23*(21), 5864-5888. http://ezproxy.library.und.edu/login?url=http://search.ebscohost.com/login.aspx?direct=true&db=keh&AN=59526789&site=ehost-live&scope=site

This article is protected by copyright. All rights reserved.

Zhang, C. (2005). Madden-Julian Oscillation. *Reviews of Geophysics, 43*(2).
https://agupubs.onlinelibrary.wiley.com/doi/abs/10.1029/2004RG000158

Accepted Article

This article is protected by copyright. All rights reserved.